Reviewed Preprint
v1 • February 24, 2026
Not revised

For correspondence:
meytal.landau@desy.de

Competing interests: No competing interests declared

Funding: See page 27

Reviewing editor: Feng Ding, Clemson University, United States



# RNA Selectively Modulates Activity of Virulent Amyloid PSMα3 and Host Defense LL-37 via Phase Separation and Aggregation Dynamics

**Bader Rayan[1], Eilon Barnea[1], Rinat Indig[1], Christian F Pantoja[2], Jesse Gayk[3], Yael Lupu- Haber[4], Alexander Upcher[5], Amir Argoetti[1], Jacob Aunstrup Larsen[6], Alexander K Buell[6], Markus Zweckstetter[2,7], Meytal Landau[1,3,8,9]**

[1]Department of Biology, Technion-Israel Institute of Technology, Haifa, Israel • [2]German Center for Neurodegenerative Diseases (DZNE), Göttingen, Germany • [3]CSSB Centre for Structural Systems Biology, Deutsches Elektronen-Synchrotron DESY, Hamburg, Germany • [4]The Life Sciences and Engineering Infrastructure Center, Technion-Israel Institute of Technology, Haifa, Israel • [5]Ilse Katz Institute for Nanoscale Science and Technology, Ben Gurion University of the Negev, Beer-Sheva, Israel • [6]Department of Biotechnology and Biomedicine, Technical University of Denmark DTU, Kongens Lyngby, Denmark • [7]Department for NMR-based Structural Biology, Max Planck Institute for Multidisciplinary Sciences, Göttingen, Germany • [8]The Center for Experimental Medicine, Universitätsklinikum Hamburg-Eppendorf (UKE), Hamburg, Germany • [9]European Molecular Biology Laboratory (EMBL), Hamburg, Germany

## eLife Assessment

This study investigates how RNA molecules modulate phase separation, aggregation, and cytotoxicity of the staphylococcal virulent peptide PSMα3 and the human host-defence peptide LL-37 using an array of biophysical and cell-based assays. If validated, these findings would be **important**, as they suggest that nucleic acids can tune the material state and bioactivity of amyloids, with implications for host-pathogen interactions and for the design of therapeutics that target phase behaviour. However, the evidence is **incomplete**: many key claims rest on qualitative imaging and contested assumptions about "functional" amyloids, and the absence of quantitative binding data, phase diagrams, and appropriate controls limits confidence in the conclusions.

https://doi.org/10.7554/eLife.109290.1.sa4

## Abstract

Amyloids, classically linked to neurodegenerative diseases, also play critical roles in infection and immunity. Phenol-soluble modulins (PSMs) from *Staphylococcus aureus* are virulent amyloids that contribute to cytotoxicity, immune modulation, and biofilm stability. PSMα3 forms cross-α amyloid fibrils and shares sequence and structural features with LL-37, a human host-defense peptide that assembles into α-helical structures. Here, we uncover RNA as a potent, context-dependent modulator of their aggregation and activity. RNA consistently reduces LL-37's cytotoxicity toward human cells without compromising its antibacterial function, suggesting a selective host-protective mechanism. In contrast, RNA preserves PSMα3's cytotoxic and antimicrobial activity over time, likely by promoting liquid–liquid phase separation (LLPS) and stabilizing bioactive fibrillar polymorphs, enabling *S. aureus* to fine-tune its virulence strategies. At higher concentrations, RNA drives both peptides toward distinct aggregated states, amorphous for LL-37 and fibrillar for PSMα3, underlying their divergent functional outcomes. The amyloid inhibitor EGCG abolishes the bioactivity of both PSMα3 and LL-37, overriding RNA's modulatory effects. Together, our findings establish RNA as a key modulator of both virulent amyloids and host-

defense peptides, with broad implications for microbial immune evasion, innate immunity, and amyloid-associated diseases. Moreover, they highlight phase transitions as a tunable mechanism for regulating peptide bioactivity and a promising therapeutic target across infectious and neurodegenerative conditions.

## Introduction

Bacterial amyloids are proteins capable of forming ordered fibrils, playing a crucial role in biofilm stability, surface adherence, cell toxicity and immune responses[1–8]. These amyloids are vital for the survival and virulence of many bacteria, enabling them to colonize and persist in diverse environments[9–11]. Some examples of bacterial amyloids include the Csg and Fap proteins from *Enterobacteria* and *Pseudomonas* species[2,7,9,12], respectively, which play a role in biofilm stability. The phenol-soluble modulins (PSMs) produced by *Staphylococci* contain amyloid-forming short peptides which play multiple functional roles central to the pathogenicity and immune evasion strategies of *S. aureus*[13–21] .

Among bacterial amyloids, PSMα3 stands out as highly cytotoxic against a broad range of microbial and human cell types[22,23]. It adopts a unique cross-α amyloid structure, where α-helices are stacked perpendicular to the fibril axis in paired sheets[22–24]. The formation of cross-α amyloids has been correlated with toxic activity, and the properties of these fibrils may regulate PSMα3's various functions[3,25,26]. PSMα3 shares self-assembly of α-helices with LL-37, a human host defense peptide[27]. Moreover, the LL-37 antimicrobial active core (residues 17–29) shows sequence similarity to PSMα3, and the formation of fibrils composed of densely packed cationic amphipathic α-helices[28]. The similarity supported the hypothesis that PSMα3 might recapitulate functions of LL-37, and indeed, they share the activation of the signal inhibitory receptor on leukocytes-1 (SIRL-1) which is a negative regulator of myeloid cell function and dampens antimicrobial responses[29]. Such common functions might be related to molecular mimicry and the ability of bacterial peptides to hijack immunomodulation pathways[30]. Indeed, PSMαs interact with the formyl peptide receptor 2 (FPR2) on immune cells, initiating immune responses such as chemotaxis, phagocytosis, and the secretion of pro-inflammatory cytokines. These reactions are critical for recruiting and activating immune cells, thereby amplifying the inflammatory response[15,31–36].

LL-37 has been shown to bind RNA released from dying cells, forming stable complexes that protect the RNA from enzymatic degradation and promote its uptake by dendritic cells[37]. Once internalized, these RNA–LL-37 complexes activate Toll-like receptors (TLRs), triggering cytokine production and dendritic cell maturation[37]. Beyond LL-37, other human antimicrobial peptides (AMPs), such as β-defensins, also form higher-order assemblies that organize nucleic acids into nanostructures with defined periodicity. These nanocomplexes potently stimulate TLRs, highlighting that innate immune activation is influenced not only by ligand identity, but also by the nanoscale geometry and spatial organization of the complexes[38–40].

Interestingly, nucleic acid interactions also play a key role in the immune activation triggered by bacterial amyloids. For example, PSMs co-assemble with extracellular DNA (eDNA), and CpG-rich DNA specifically promotes PSMα3 fibrillation, forming co-aggregates that colocalize with DNA in biofilms. These complexes activate TLR pathways and induce anti-dsDNA autoantibody responses in mice[41]. Similar mechanisms are seen in *E. coli* and *Salmonella*, where curli fibers bind eDNA, enhance fibrillation, and engage TLRs signaling, also promoting autoimmunity[42,43]. These findings suggest that amyloid–DNA complexes in bacterial biofilms are not only structural components but also potent immunomodulators with potential links to autoimmunity.

The similarities between LL-37 and PSMα3 prompted us to investigate their interaction with RNA and the resulting structural and functional implications on cell toxicity. Our findings show that both PSMα3 and LL-37 can undergo liquid-liquid phase separation (LLPS) in the presence of RNA, and transition into solid aggregates as a function of incubation time and RNA concentration. LLPS is in general a critical process in cellular organization in which proteins or other molecules separate into distinct liquid phases, forming dynamic, membraneless compartments central to

cellular processes such as metabolism, RNA regulation, and stress response[44–47]. PSMα3 also penetrates HeLa cells, localizes within the nucleolus, and colocalizes with nucleic acids. We observed dynamic and reversible molecular behavior within the nucleolus, mirroring in vitro observations of PSMα3's LLPS with RNA.

Epigallocatechin gallate (EGCG), a polyphenol primarily found in green tea and recognized as an amyloid inhibitor[4,48–50], disrupts the cytotoxicity and antibacterial activity of both PSMα3 and LL-37. In contrast, RNA differentially modulates their activity, suggesting distinct mechanisms linked to their self-assembly dynamics, morphologies, and toxic pathways. These findings provide new insights into RNA-mediated self-assembly in bacterial physiology and highlight potential biomedical applications for combating resistant *S. aureus* infections.

# Results

## PSMα3 interacts with RNA in vitro

The interactions between PSMα3 and RNA were assessed using an Electrophoretic Mobility Shift Assay (EMSA), comparing the binding affinity of PSMα3 to single-stranded PolyA RNA and double-stranded Poly (AU) RNA. The RNA molecules were labeled with the IR800CW fluorescent dye (as detailed in the Methods section). Freshly dissolved PSMα3, at varying concentrations, was incubated with each RNA type at a constant concentration for 30 minutes at 37°C. The EMSA results revealed that PSMα3 exhibits a stronger binding affinity to double-stranded Poly (AU) RNA, as evidenced by significant shifts at lower peptide concentrations compared to single-stranded Poly(A) (Fig. 1A).

A high density of PSMα3 fibrils was observed after 2 hours of incubation with Poly (AU) RNA using transmission electron microscopy (TEM), while incubation with Poly(A) RNA under the same conditions resulted in amorphous aggregation (Fig. 1B). Consequently, we decided to focus our subsequent investigations on the behavior of PSMα3 in the presence of double-stranded Poly (AU) RNA.

## Poly (AU) RNA concentration-dependent induced transitioning of PSMα3 condensates to solid aggregates

To better understand the nature of the PSMα3-RNA interaction, we visualized their mixtures via fluorescence microscopy, using PSMα3 labeled with Fluorescein isothiocyanate (FITC) at the C-terminus (PSMα3-FITC), which is known to form fibrils[22]. 100 μM PSMα3-FITC was incubated with either 50 ng/μl or 400 ng/μl propidium iodide (PI)-labeled RNA in a close to physiological buffer of 50 mM HEPES (pH 7.4) containing 150 mM sodium chloride (NaCl).

With the addition of 50 ng/μl RNA, PSMα3 formed liquid-liquid phase separated droplets that clearly colocalized with the RNA (Fig. 2A). The liquid nature of the droplets was further validated by fluorescence recovery after photobleaching (FRAP) analysis, where we observed a rapid recovery of the PSMα3-FITC signal shortly after bleaching (Fig. 2C). However, after a longer incubation of 2 hours, no fluorescence recovery was detected, suggesting that the condensates aged and transitioned to a more aggregated state (Fig. 2D). In addition, we observed the encapsulation of RNA within PSMα3-FITC "coated" droplets (Fig. S1).

In contrast to the effect of 50 ng/μl RNA, the addition of a higher RNA concentration of 400 ng/μl to PSMα3 resulted in immediate aggregation, with no observed phase of droplet formation (Fig. 2B). FRAP analysis indicated no recovery of signal after bleaching, likely due to the formation of solid structures rather than droplets with liquid-like properties (Fig. 2E). These aggregates also showed colocalization (Fig. 2B), indicating that the PSMα3-RNA interaction persisted in both the LLPS and solid states.

Turbidity assays showed that a 30 min co-incubation of 100 μM PSMα3 with varying concentrations of RNA displayed an increased turbidity up to 50 ng/μl, while higher RNA concentrations displayed a decrease in turbidity (Fig. S2). This suggests that 50 ng/μl can be a critical concentration between soluble species, which might be able to phase separate, and the

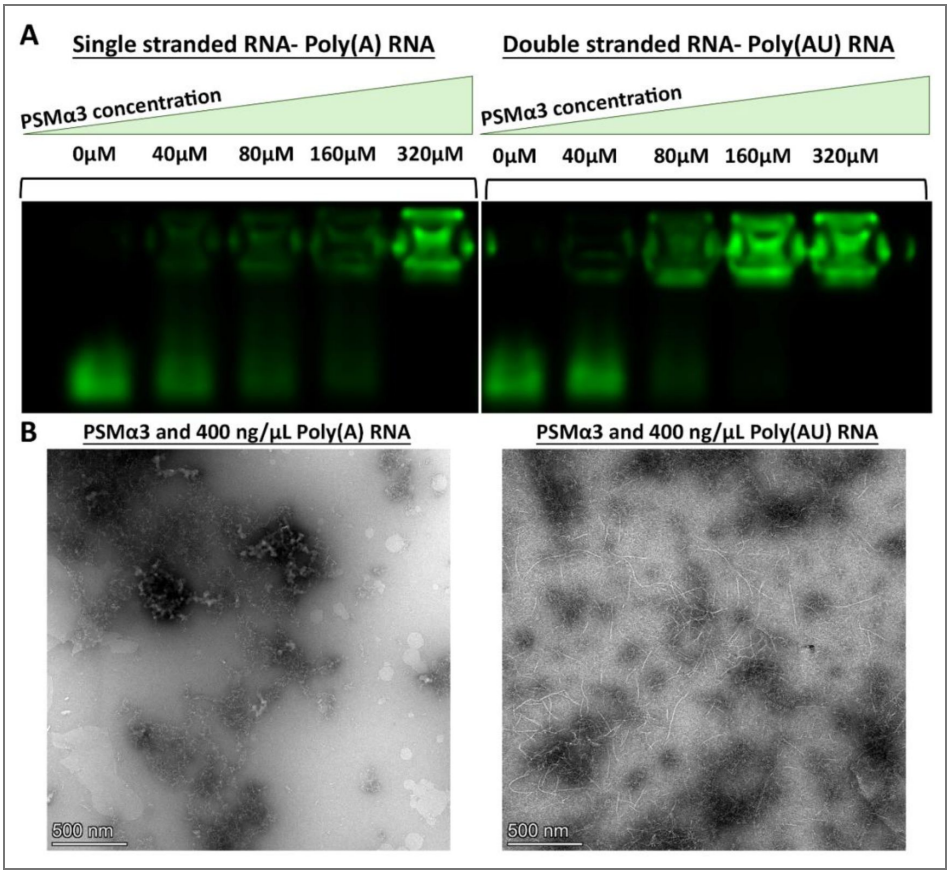


**Figure 1. The binding and effect of single- and double-stranded RNA on PSMα3.**

**(A)** EMSA assay illustrating the interaction between PSMα3 and RNA. The assay compares the effects of increasing concentrations of PSMα3 (0 μM, 40 μM, 80 μM, 160 μM, and 320 μM), shown in a gradient from left to right, on the mobility shift of single-stranded Poly(A) RNA (left panel) and double-stranded Poly (AU) RNA (right panel) at ~400ng/μL. **(B)** Transmission electron micrographs of 100 μM PSMα3 incubated for 2 hours in the presence of 400 ng/μL of either Poly(A) RNA (left) or Poly (AU) RNA (right). Scale bars represent 500 nm.

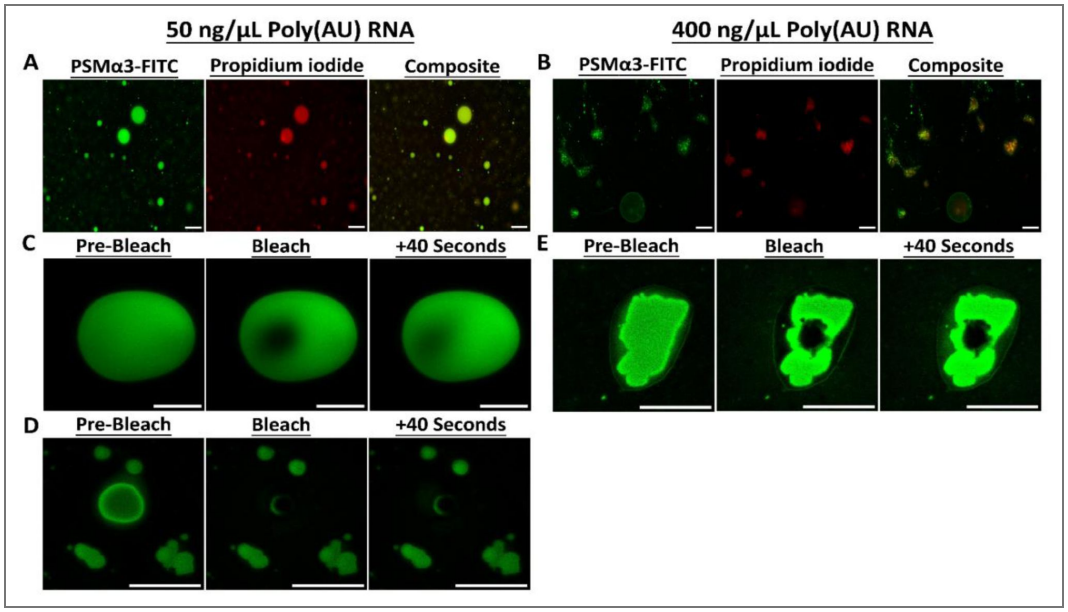


**Figure 2. Colocalization, droplet formation and texture of PSMα3 mixed with varying Poly (AU) RNA concentrations.**

**(A-B)** Widefield fluorescence microscopy images of 100 µM PSMα3-FITC (green) in the presence of 50 ng/µL (**A**) or 400 ng/µL (**B**) Poly (AU) RNA (red), showing their individual and composite channel images. (**C-E**) FRAP analysis of PSMα3-FITC with 50 ng/µL Poly (AU) RNA taken after 10 min (**C**) or 2-hours co-incubation (**D**), or with 400 ng/µL Poly (AU) RNA taken after 10 min co-incubation (**E**). The images in panels C-D were captured before bleaching, immediately after bleaching, and 40 seconds post-bleaching. Scale bars in all images represent 20 µm.

formation of aggregates. The decrease in particle size above 50 ng/μL can be a result of either the formation of smaller particles or aggregation into larger clusters, which can settle out of suspension, removing them from the light-scattering medium and reducing turbidity.

Alternatively, it may indicate the dissolution of phase-separated droplets, as observed in systems like Ddx4[51]. We then used transmission electron microscopy (TEM) and total internal reflection fluorescence (TIRF) microscopy to better visualize the effect of RNA on PSMα3 morphology.

## RNA concentration-driven changes in PSMα3 fibrillar morphology and aggregation

The TEM micrographs showed that in the absence of RNA, 100 μM PSMα3 formed nanotube-like fibrils after 2 hours, growing wider or with some twist after 24-hours co-incubation (Fig. 3A). Incubating PSMα3 with a low concentration of 10 ng/μL RNA displayed accelerated fibril formation, with more strongly twisted, wide, sheet-like fibrils observed after both 2 hours and 24 hours (Fig. 3A). With the addition of 50 ng/μL RNA, PSMα3 fibrils have a similar twisted morphology after 2 hours, while at a longer incubation time of 24 hours, we observed a significant morphological shift into more thin amorphous aggregates (Fig. 3A). At the higher concentration of 400 ng/μL RNA, PSMα3 formed dense, thin fibrils after 2 hours, but with a possible fragmentation into smaller species or rearrangement into amorphous aggregates after 24 hours of co-incubation. This indicates that RNA concentration and time of co-incubation affect the density and morphology of PSMα3 fibrils. This corresponds to the differences observed by light microscopy of co-aggregates contexture of LLPS droplets vs solid aggregates (Fig. 2).

These observations were further supported by TIRF microscopy using the amyloid-specific dye AmyTracker630 (AT630). TIRF analysis was performed at 50 ng/μL and 400 ng/μL RNA, which induced phase separation and solid aggregation of PSMα3, respectively. With the addition of 50 ng/μL RNA to PSMα3-FITC, a strong AT630 fluorescence signal was detected after 2 hours co-incubation, but not after 30 minutes. This suggests a time-dependent transition into amyloid-like species (Fig. 3B). Conversely, at 400 ng/μL RNA, a significant AT630 fluorescence was observed already after 30 minutes of co-incubation, consistent with a rapid formation of amyloid fibrils (Fig. 3C). These findings highlight a concentration- and time-dependent modulation of PSMα3 phase separation and structural transitions, where RNA promotes LLPS at lower concentrations and drives rapid amyloid formation and unique fibrillar morphologies at higher concentrations.

Solid-state circular dichroism (ssCD) spectroscopy reveals that PSMα3 lacks a defined secondary structure both immediately after preparation and following 2 hours of incubation. However, upon addition of RNA, a clear shift toward an α-helical conformation is observed (Fig. S3). This supports the notion that RNA not only accelerates aggregation but also promotes or stabilizes the α-helical fibrillar architecture, potentially consistent with cross-α amyloid structures.

## RNA modulates the antibacterial activity of PSMα3

The antimicrobial activity of PSMα3 against *Escherichia coli* was evaluated under varying RNA concentrations and incubation times using the PrestoBlue Cell Viability Assay (Fig. 4A).

Freshly dissolved 10 μM PSMα3 exhibited potent antibacterial activity, completely abolishing bacterial viability. After 2 hours of incubation, PSMα3 retained its full activity, comparable to its freshly prepared state. The presence of RNA at 50 ng/μL and 400 ng/μL had no impact on its antimicrobial function within this timeframe (Fig. 4A).

In contrast, after 24 hours of incubation, PSMα3's antibacterial activity was significantly reduced (Fig. 4A), also at 20 μM, suggesting a decrease in its effective concentration or changes in its morphology. Notably, the addition of RNA at 50 ng/μL or 400 ng/μL prevented this loss of activity, indicating that RNA plays a stabilizing role of toxic species. These findings suggest that RNA influences PSMα3 aggregation dynamics and morphology, thereby modulating its long-term antimicrobial effectiveness.

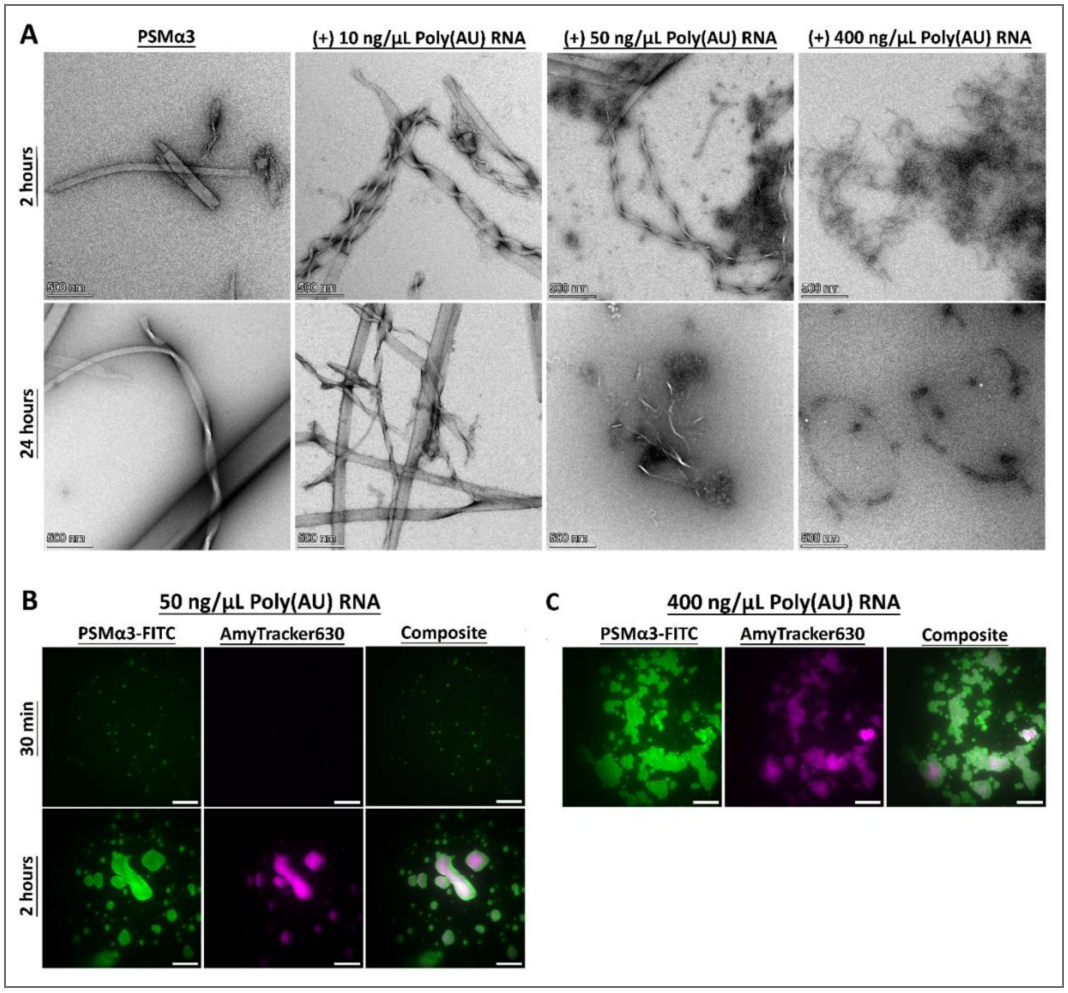


**Figure 3. TEM and TIRF visualization of PSMα3 aggregation and morphology with different Poly (AU) RNA concentrations and incubation times.**

**(A)** TEM micrographs of 100 μM PSMα3 incubated with or without Poly (AU) RNA at varying concentrations of 10 ng/μL, 50 ng/μL, and 400 ng/μL for 2 hours (top row) and 24 hours (bottom row). Scale bars represent 500 nm. **(B)** TIRF microscopy images showing 100 μM FITC-PSMα3 (green) co-incubated with 50 ng/μL Poly (AU) RNA and the amyloid indicator AT630 (magenta) for 30 minutes and 2 hours. Scale bars represent 20 μm. **(C)** TIRF microscopy images of 100 μM FITC-PSMα3 (green) co-incubated with 400 ng/μL Poly (AU) RNA and AT630 (magenta) for 30 min. Scale bars represent 20 μm.

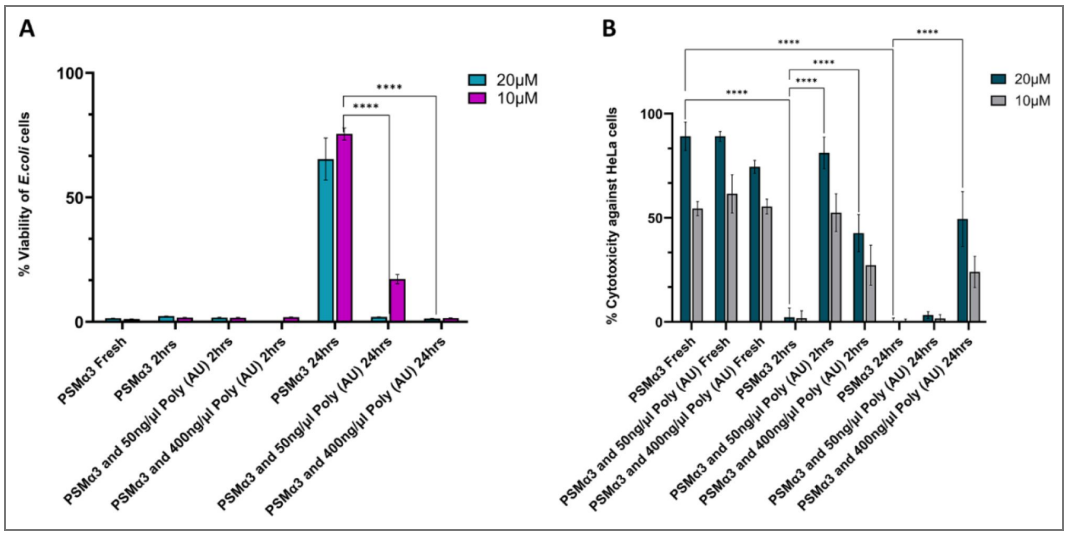


**Figure 4. Impact of Poly (AU) RNA on PSMα3 cytotoxicity and antibacterial activity.**

Antimicrobial activity of PSMα3 against *E. Coli* using the PrestoBlue cell viability assay (**A**) and its cytotoxicity against HeLa cells using the LDH colorimetric assay (**B**) were assessed with and without Poly (AU) RNA at varying concentrations. The experiments were performed in at least three replicates and repeated across three independent days to ensure result reliability. Cytotoxicity and bacterial cell viability percentages were calculated as the mean of all replicates, with error bars representing the standard error of the mean (SEM). Statistical significance was determined using one-way ANOVA for normally distributed data in GraphPad Prism (version 11). Significance levels are indicated as follows: *p<0.05, **p<0.01, ***p<0.001, ****p<0.0001.

## RNA modulates PSMα3 cytotoxicity against human HeLa cells

The effect of RNA on the cytotoxicity of PSMα3 against human HeLa cells was evaluated by measuring lactate dehydrogenase (LDH) release, an indicator of cell membrane damage (Fig. 4B). Freshly dissolved PSMα3 exhibited substantial cytotoxicity, causing approximately 80% cell death at 20 μM and 50% at 10 μM. The presence of RNA did not significantly alter the toxicity of freshly dissolved PSMα3 (Fig. 4B), similar to the antibacterial activity. However, following 2 hours of incubation, PSMα3 cytotoxicity was significantly reduced, possibly due to aggregation and a loss of active peptide concentration. This reduction occurred earlier than the loss of antibacterial activity, which was only observed after 24 hours of incubation (Fig. 4A). This discrepancy may reflect differences in how membrane composition and media conditions influence PSMα3 aggregation kinetics, or it may indicate distinct mechanisms underlying cytotoxicity versus antibacterial membrane disruption.

Notably, co-incubation with RNA helped maintain PSMα3 cytotoxicity in a concentration-dependent manner. With 50 ng/μL RNA, the 2-hour incubated PSMα3 retained cytotoxicity comparable to its freshly dissolved form, suggesting that RNA prevents activity loss due to incubation. However, after 24 hours, 50 ng/μL RNA was insufficient to preserve cytotoxicity.

In contrast, at 400 ng/μL RNA, partial cytotoxicity was maintained for both 2-hour and 24-hour incubated PSMα3, compared to the freshly dissolved sample.

Overall, these findings suggest that RNA prevents the incubation-induced loss of both antibacterial activity and cytotoxicity (Fig. 4). This effect appears to be concentration- and co-incubation time-dependent, likely linked to RNA-induced morphological variations of PSMα3 species (Figs. 2&3).

## PSMα3 targets nucleolar nucleic acids in HeLa cells with LLPS dynamics

The interactions and localization of PSMα3 were next explored in HeLa cells with the addition of 20μM FITC-PSMα3 just before imaging. PI was added to the cell medium as a marker for cell death, as it selectively penetrates dead cells and binds to their nucleic acids.

Confocal microscopy images revealed that PSMα3 induces significant toxicity as indicated by membrane damage, intracellular PSMα3 aggregate formation, and positive PI staining. PSMα3 also enters the nuclei, with a notable concentration in the nucleolus, indicated by the foci of green fluorescence (marked by white arrows in Fig. 5). The composite images demonstrated clear colocalization of PSMα3 with nucleic acids in the nucleolus, as seen by the overlap of the green PSMα3-FITC signal and the red fluorescence from PI-stained nucleic acids.

FRAP analysis of 20 μM PSMα3-FITC within the nucleolus of HeLa cells indicated mobility (Fig. 5B). The Pre-bleach panel shows the initial fluorescence distribution, with the nucleolus marked by the white arrow. Following photobleaching, a localized reduction in fluorescence was observed. Notably, within 60 seconds, significant fluorescence recovery was observed in the nucleolus, highlighting the dynamic and reversible molecular behavior of PSMα3 in this cellular compartment. The results overall suggest an interaction between PSMα3 and nucleolar RNA/DNA within cells, which mirrors our in vitro findings where PSMα3 interacted, and underwent LLPS and formed solid aggregates in the presence of RNA.

## EGCG directly binds PSMα3 and inhibits its fibrillation and bioactivity, even in the presence of RNA

Since RNA appears to protect or maintain PSMα3's toxic functions, potentially by influencing its fibril formation and morphology, we investigated the corresponding and combined effects of an inhibitor of fibril formation. One such inhibitor is epigallocatechin gallate (EGCG), the most abundant catechin in tea and a known amyloid inhibitor, including of PSMs[4].

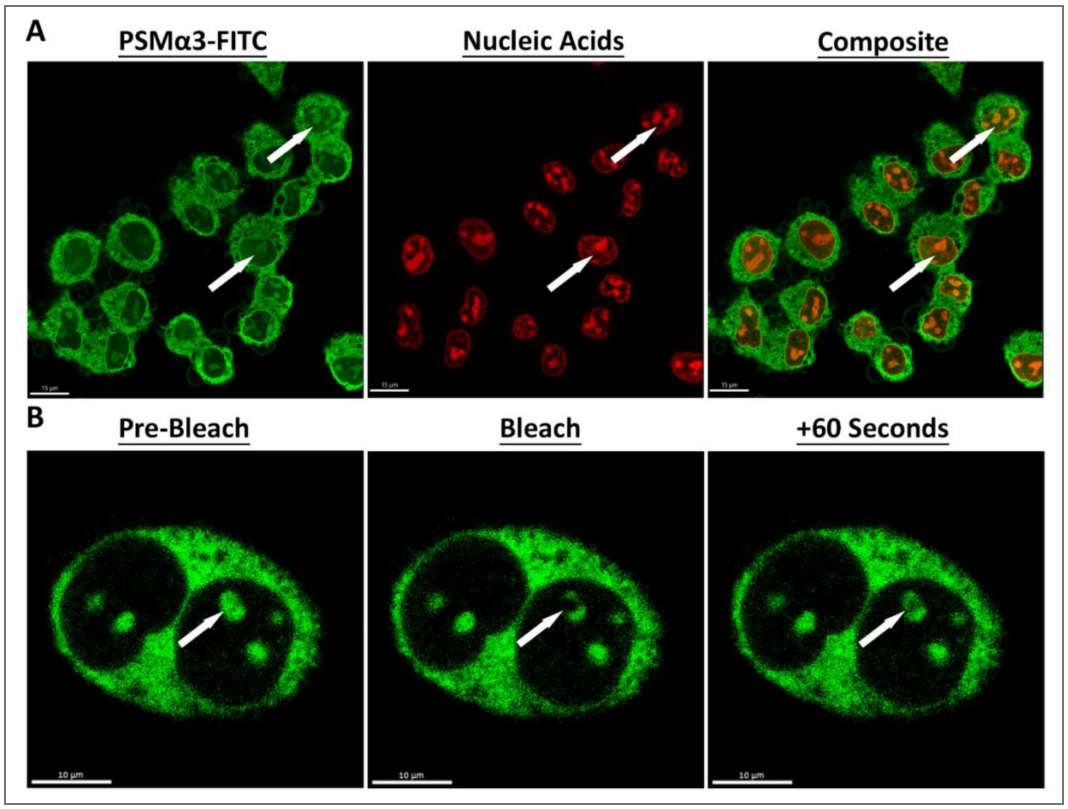


**Figure 5. Colocalization of PSMα3 with nucleic acids in HeLa cells.**

**(A)** Confocal microscopy images showing the localization and colocalization of 20 μM PSMα3-FITC (green) and nucleic acids stained with PI (red) inside the nucleolus of HeLa cells (indicated in arrows). The left panel illustrates the distribution of PSMα3 within the cell. The middle panel shows the nucleic acids stained with PI. The right panel is a composite image that demonstrates the colocalization of PSMα3 with nucleic acids. Scale bars represent 15 μm. **(B)** FRAP analysis of 20 μM FITC-labeled PSMα3 inside the nucleolus (indicated by the arrow) of HeLa cells, showing fluorescence recovery after 60 seconds. Scale bars represent 10 μm.

The addition of EGCG to PSMα3 at a 1:1 molar ratio did not significantly alter its cytotoxicity against HeLa cells. However, at a fivefold molar excess, EGCG completely abolished PSMα3's cytotoxic effect (Fig. 6C). To examine the structural changes underlying this effect, we analyzed fibril formation kinetics and morphology in the presence of EGCG. TEM micrographs revealed that a fivefold molar excess of EGCG disrupted fibril formation of 100 μM PSMα3, instead inducing amorphous aggregates (Fig. 6A). Consistently, kinetics assays of fibril formation showed that EGCG inhibited the Thioflavin-T (ThT) fluorescence curve otherwise indicating the fibril formation of 100 μM PSMα3 (Fig. S4). These findings suggest that EGCG reduces PSMα3 toxicity by modulating its fibril formation and morphology. The addition of RNA did not counteract the effect of EGCG or restore PSMα3 cytotoxicity (Fig. 6C), highlighting the strong impact of EGCG on PSMα3 morphology and properties.

To investigate residue-specific interactions between PSMα3 and EGCG, we performed NMR spectroscopy using a 2:1 PSMα3:EGCG molar ratio. The 1D $^{1}$H-NMR spectrum revealed distinct chemical shift changes and peak broadening upon EGCG addition, particularly in residues Glu8/Met1 and Glu2, suggesting specific interactions between these sites and the EGCG molecule (Fig. 7A). Peak broadening was also observed in the aromatic region of EGCG, especially for protons H1 and H2, compared to the reference spectrum of EGCG alone, indicating that the interaction is visible from the EGCG side as well. Notably, slight opalescence was observed in the sample following preparation, potentially reflecting early-stage aggregate formation. Additionally, the presence of multiple cross-peaks between non-sequential residues (i+3 or i+4) in the two-dimensional (2D) $^{1}$H-$^{1}$H Nuclear Overhauser Effect Spectroscopy (NOESY) spectrum indicates a well-defined structure of PSMα3 in this condition (Fig. 7B). The 2D $^{1}$H-$^{1}$H Total Correlation Spectroscopy (TOCSY) spectrum displayed connectivity between backbone amide (HN) and alpha protons (Hα) for several assigned residues, while the 2D $^{1}$H-$^{1}$H NOESY spectrum revealed spatial correlations between nearby residues (i+1).

To assess the temporal stability of the sample, we monitored signal intensities over a 3-day period. PSMα3 signals remained stable, with only a ~10% decrease in intensity, whereas EGCG signals exhibited substantial degradation, with nearly 50% loss over the same time frame (Fig. 7C). Given the ~1.5-day duration of the 2D NMR measurements, it is estimated that over 60% of EGCG remained in solution during data acquisition, allowing for reliable observation of its interaction with the peptide. Of note, EGCG's activity has been shown to depend on its chemical stability and the surrounding conditions. Specifically, at neutral pH, EGCG may undergo oxidation, and its inhibitory effects could be attributed to its degradation products rather than the intact compound itself[52].

Live-cell confocal microscopy provided further insights into how EGCG binding affect PSMα3 interactions with cells. A fivefold molar excess of EGCG prevented the toxic effects of 20 μM PSMα3, blocking cell penetration and PI staining (Fig. 6B, top panel). Instead, PSMα3-FITC formed extracellular aggregates and showed no interaction with cell membranes, as indicated by the absence of PI staining and intact cell membranes (Fig. 6B, bottom panel).

Furthermore, EGCG at a fivefold molar excess also reduced the antibacterial activity of PSMα3 against *E. coli*, maintaining bacterial cell viability (Fig. S5). Super-resolution fluorescence microscopy showed that while 20 μM PSMα3 typically aggregates on the bacterial membrane, causing membrane disruption and PI staining indicative of cell death (Fig. S5), EGCG at a fivefold molar excess prevented membrane aggregation and PI staining, thereby preserving membrane integrity.

## RNA modulates the human host defense peptide LL-37 phase behavior and cytotoxicity without compromising antimicrobial activity

LL-37, a human host defense peptide, shares functional, sequence, and structural similarities with PSMα3, including its ability to self-assemble and interact with nucleic acids[28,37]. We therefore examined whether RNA similarly influences LL-37 activity and properties.

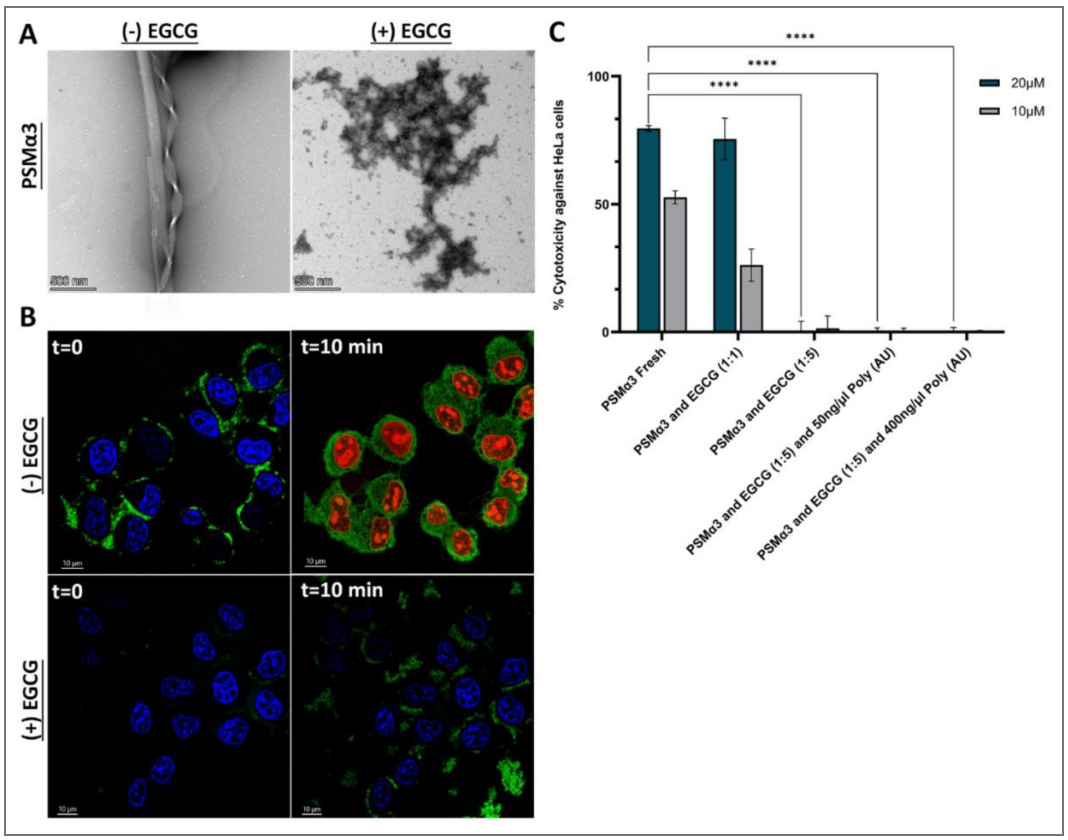


**Figure 6. EGCG modulates PSMα3 aggregation and reduces toxicity against HeLa cells.**

(**A**) TEM micrographs of 100 μM PSMα3 incubated for 24 hours, without (left) and with (right) a fivefold molar excess of EGCG. Scale bars: 500 nm. (**B**) Live-cell confocal microscopy of HeLa cells treated with 20 μM PSMα3-FITC (green) without (top) and with EGCG (bottom), imaged immediately after preparation (t = 0) and after 10 minutes. Hoechst 33342 (blue) marks the nuclei, while PI staining (red) indicates membrane disruption. Scale bars: 10 μm. (**C**) Cytotoxicity of PSMα3 against HeLa cells in the presence and absence of EGCG and Poly (AU) RNA at two different concentrations, assessed via LDH assay. The experiment was performed in triplicate and repeated on three separate days for consistency. Cytotoxicity percentages were averaged across all replicates, with error bars representing the standard error of the mean. Statistical significance: *p < 0.05, **p < 0.01, ***p < 0.001, ****p < 0.0001 (one-way ANOVA, GraphPad Prism v11).

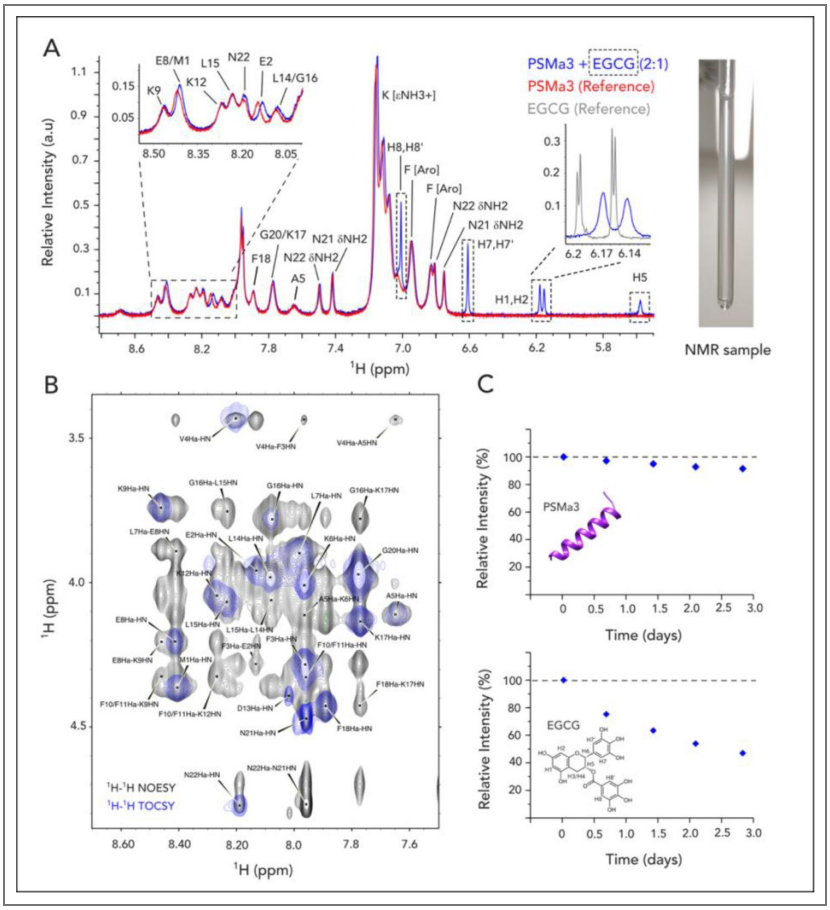


**Figure 7. Residue-specific interactions between PSMα3 and EGCG.**

(**A**) One-dimensional (1D) $^{1}$H NMR spectra of 1.0 mM PSMα3 alone (red) and in complex with 0.5 mM EGCG (blue), recorded at 35 °C. Specific residues, including Glu8/Met1 and Glu2, show chemical shift changes suggestive of direct interaction with EGCG (highlighted in the upper left). Dashed boxes mark proton signals corresponding to EGCG. Peak broadening of H1/H2 protons, compared to the EGCG-only reference sample (light gray), indicates interaction from the EGCG side. Slight opalescence observed in the sample suggests potential aggregate formation. (**B**) Two-dimensional (2D) $^{1}$H–$^{1}$H TOCSY and NOESY spectra of the PSMα3:EGCG complex at a 2:1 ratio, recorded at 35 °C. The cross-peaks in the TOCSY spectrum allow the identification of the spin system and direct connections through the scalar coupling between the proton amide (HN) and the alpha protons (Hα) of the same residue. The cross-peaks in the NOESY spectrum establish a sequential connection between neighboring residues (i+1), allowing spectral assignment. The remaining cross-peaks (i+3 or i+4) in the spectrum support PSMα3 secondary structure in the experimental conditions. (**C**) Temporal stability of the PSMα3:EGCG sample over 3 days.

Fluorescence microscopy showed that 100 μM LL-37-FITC incubated with 100 ng/μL PI-labeled Poly (AU) RNA displayed formation of aggregates, but with no indication for LLPS or droplet formation (Fig. S6). Since diverse stresses trigger phase separation of RNA-binding proteins and their coalescence into stress granules[53], we explored the effect of RNA on LL-37 under thermal stress. We applied heat shock at 65°C for 15 minutes and found that RNA significantly affected LL-37's phase behavior in a concentration-dependent manner. Specifically, with the addition of 100 ng/μL RNA, LL-37 formed condensates that colocalized with the RNA (Fig. 8A). At 200 ng/μL RNA, LL-37 still formed droplets, but aggregation began to appear, indicating a transition from a liquid-like state to a more solid-like phase (Fig. 8B). At 400 ng/μL RNA, droplets were no longer observed, and extensive aggregation occurred, with strong colocalization between LL-37 and RNA (Fig. 8C). As a comparison of stress response, PSMα3 displayed droplet formation after the heat shock of 65°C for 15 minutes only at more conducive conditions of pH 4, but not at pH 7.4 (Figs. S7-S8). The results overall suggest that for both LL-37 and PSMα3, higher RNA concentrations promote aggregation over phase separation.

Freshly dissolved LL-37 exhibited cytotoxicity against HeLa cells, which, in contrast to PSMα3, remained consistent even after incubation for up to 24 hours. Notably, RNA significantly reduced LL-37 cytotoxicity in a concentration-dependent manner, irrespective of the incubation duration (freshly dissolved, 2 hours, or 24 hours) (Fig. 8D). This contrasts with RNA's rescuing effect on the incubation time-dependent loss of PSMα3 cytotoxicity. The antimicrobial activity of LL-37 against *E. coli* also remained unchanged upon incubation. However, unlike its effect on cytotoxicity, RNA had minimal impact on antibacterial activity, with only high concentrations of 400 ng/μL reducing LL-37 activity (Fig. 8E). Similar to PSMα3, LL-37 cytotoxicity against HeLa cells and its antimicrobial activity was attenuated by EGCG in a concentration-dependent manner (Fig. 8E).

TEM micrographs of 100 μM LL-37 revealed a variety of aggregative and fibrous structures, including thin, curli-like fibrils, although no consistent morphology was observed (Fig. S9A). RNA induced a distinct morphological change, leading to increased aggregation and the formation of mostly amorphous species, but also some thicker, ribbon-like fibrils were observed. These structures resemble those previously observed for a segment of the LL-37 active core (residues 17–29), which is similar to PSMα3 in sequence and its ability to form fibrils of densely packed amphipathic α-helices[28]. Heat shock further intensified aggregation, resulting in denser, amorphous condensates and larger fibrillar assemblies, with and without RNA (Fig. S9B). The distinct effects of RNA on the aggregation and morphologies of LL-37 and PSMα3 may underlie the observed differences in their cytotoxic and antibacterial activities.

## Discussion

This study demonstrates that Poly (AU) RNA modulates the cytotoxic and antimicrobial activities of PSMα3 and LL-37 in a concentration-dependent and peptide-specific manner, revealing a regulatory mechanism that differentially influences their biological functions. The effects of RNA on these peptides are distinctly linked to their aggregation dynamics and morphological outcomes, underscoring its role as a context-specific modulator of peptide bioactivity.

Interestingly, although the supramolecular structure of LL-37 does not exhibit the characteristic amyloid cross-β or the cross-α architecture, with molecular stacking perpendicular to the fibril axis[27], it nonetheless shows functional links to amyloids. Notably, LL-37 has been reported to bind the Alzheimer's-associated amyloid-β (Aβ) peptide and inhibit its fibrillization, likely by stabilizing prefibrillar intermediates[54]. These findings suggest that LL-37 may modulate Aβ aggregation dynamics, with potential implications for aging, immune suppression, and infection[54].

Our findings demonstrate that RNA consistently reduces LL-37's cytotoxicity against human cells, independent of RNA concentration or incubation duration (Fig. 8D). Notably, this reduction in cytotoxicity does not compromise LL-37's antimicrobial activity against *E. coli* (Fig. 8E), indicating that RNA selectively protects mammalian cells while preserving its host defense functions. Unlike PSMα3, LL-37 does not undergo RNA-induced LLPS under physiological

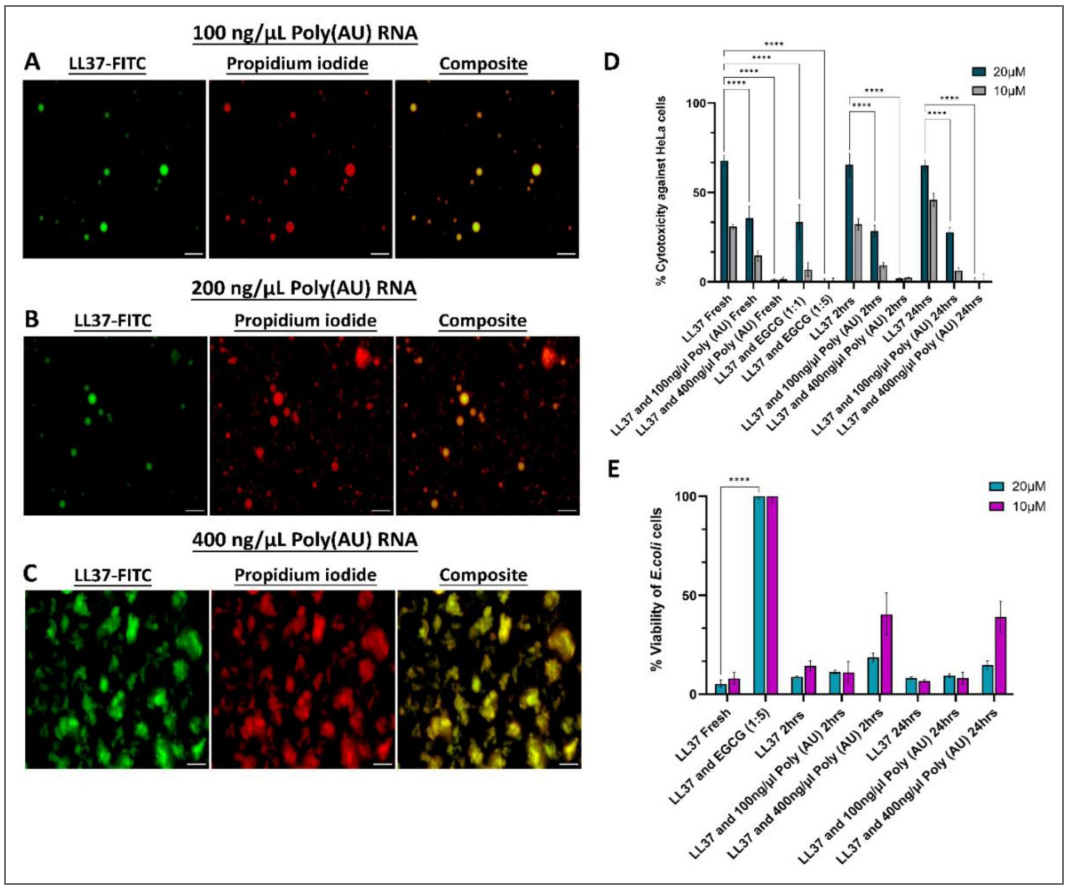


**Figure 8. Effect of RNA concentration on LL37 phase separation, aggregation, and activity at pH 7 after heat shock.**

Fluorescence microscopy images showing LL37 (FITC-labeled, green) in the presence of increasing concentrations: 100 ng/µL (**A**), 200 ng/µL (**B**) and 400 ng/µL (**C**) of Poly (AU) RNA (PI-labeled, red) after heat shock at 65°C for 15 minutes at pH 7. Scale bars represent 20 µm. **(D)** LL37 cytotoxicity, with and without Poly (AU) RNA and EGCG at varying concentrations, was assessed in HeLa cells using the LDH colorimetric assay. The experiment was performed in triplicate and repeated on three separate days for reproducibility. Cytotoxicity percentages represent the average of all replicates, with error bars indicating the standard error of the mean. **(E)** The antimicrobial activity of LL37, with and without Poly (AU) RNA and EGCG at varying concentrations, was evaluated against *E. coli* using the PrestoBlue Cell Viability assay. The experiment was performed in triplicate and repeated on three separate days for reproducibility. Bacterial viability percentages represent the average of all replicates, with error bars indicating the standard error of the mean. Statistical significance (**D-E**): *p < 0.05, **p < 0.01, ***p < 0.001, ****p < 0.0001 (one-way ANOVA, GraphPad Prism v11).

conditions, exhibiting this behavior only after thermal stress (Fig. 8). RNA rather leads to amorphous aggregates (Fig. S9), which likely underlies the selective attenuation of cytotoxicity, highlighting RNA's role in modulating LL-37's functional states.

In contrast to the results for LL-37, RNA exhibits a dynamic and concentration-dependent regulation of PSMα3's cytotoxicity and antimicrobial activity, revealing a complex interplay between phase separation and aggregation. Unlike LL-37, PSMα3 shows a time-dependent reduction in activity (Fig. 4), likely due to a transition from soluble species to irreversible fibril morphology (Fig. 3). At lower RNA concentrations, PSMα3's cytotoxic activity against human cells is initially preserved but diminishes over time. This time-dependent decrease likely reflects a transition from soluble liquid-like droplets to solid aggregates within the RNA-PSMα3 complex. Conversely, at higher RNA concentrations, PSMα3's cytotoxicity is partially maintained even after prolonged incubation, suggesting that RNA induces a specific fibril morphology that remains reversible and bioactive.

The antimicrobial activity of PSMα3 also shows temporal modulation, with a noticeable decline after 24 hours of incubation (Fig. 4A). This delayed reduction compared to its activity against human cells suggests distinct aggregation pathways or interactions with the bacterial environment. However, RNA preserves PSMα3's antimicrobial function even after 24 hours (Fig. 4A), likely by stabilizing intermediate or alternative polymorph states, which are reversible and enable the reactivation of PSMα3.

This behavior of dynamic phase transitions and aggregation mirrors those observed in human amyloids[45,46,55–64]. For example, FUS, TDP-43, hnRNPA1, and tau rely on LLPS to perform their normal cellular functions. However, these proteins are also associated with neurodegenerative diseases like amyotrophic lateral sclerosis, frontotemporal dementia, tauopathies, and Alzheimer's disease. While LLPS enables their proper functioning under healthy conditions, mutations or modifications can disrupt this process, leading to irreversible aggregation and disease progression[55–66]. Similar to human amyloids, AMPs can also induce LLPS with nucleic acids[67]. In bacterial cells, this interaction compacts nucleic acids and disrupts critical processes like transcription and translation[67]. PSMα3 interaction with nucleic acids within human cells, particularly its localization in the nucleolus (Fig. 5), supports a comparable mechanism leading to cell death mediated by this bacterial virulence factor.

These findings reveal a sophisticated and context-specific regulation of PSMα3 and LL-37 by RNA, demonstrating that RNA can fine-tune peptide bioactivity with remarkable specificity across cell types. The specificity of RNA's effects on cytotoxicity and antimicrobial activity points to a sophisticated regulatory mechanism with significant biological implications: For PSMα3, RNA-driven LLPS and aggregation dynamics provide a flexible strategy for modulating cytotoxicity and antimicrobial activity, enabling *S. aureus* to adapt its virulence based on environmental cues. This dynamic structural plasticity may facilitate immune evasion, biofilm formation, and enhanced survival in diverse host environments. For LL-37, RNA's selective attenuation of cytotoxicity without compromising antibacterial function suggests an evolutionary strategy to balance host defense and tissue protection. This regulatory mechanism minimizes collateral damage to host cells while maintaining effective antimicrobial activity, highlighting dual functionality in immune regulation.

These findings reveal a previously unrecognized role for RNA in regulating amyloid-like peptides, opening new avenues for RNA-targeted therapeutic interventions against bacterial infections and immune regulation. Moreover, the parallels between RNA-driven phase transitions in PSMα3 and human amyloids suggest broader implications for understanding amyloid-associated diseases. By elucidating the dual role of RNA in promoting reversible LLPS and inducing stable fibril formation, this study contributes to the growing understanding of phase behavior in functional and pathological amyloids.

# Methods

## Peptide and Poly (AU) RNA preparation

Unlabeled and C-terminal FITC-labeled PSMα3 and LL-37 (PSMα3-FITC and LL-37-FITC) (>98% purity) were purchased from GL Biochem (Shanghai) Ltd. Poly (AU) RNA was purchased from Sigma Aldrich. A stock solution of the peptides was prepared at a concentration of 1 mM in a mixture of 20% dimethyl sulfoxide (DMSO) and 80% ultra-pure water. For light microscopy experiments, we used a mixture of 20% FITC-labeled and 80% unlabeled PSMα3 or LL-37. The Poly (AU) RNA stock solution was prepared at a concentration of 2000 ng/µl in UPW, the stock solution was stored at −80 °C until further use. Labeled Poly (AU) RNA was prepared by introducing 0.02 mg/ml of PI dye to the Poly (AU) RNA stock solution. For the experiments, samples containing 100 µM PSMα3 or LL-37 with Poly (AU) RNA at 10, 50, 100, 200, or 400 ng/µl were prepared in 50 mM HEPES buffer with 150 mM sodium chloride (NaCl), adjusted to pH 7.4, or in 20 µM Tris, 20 µM Bis-Tris, and 20 µM sodium acetate adjusted to pH 4.

## Cytotoxicity against HeLa cells tested using the lactate dehydrogenase (LDH) release assay

Human cervical carcinoma HeLa cells (ATCC® CCL-2™) were routinely cultured in Dulbecco's Modified Eagle's Medium - high glucose (DMEM) (Sigma, Israel) with L-glutamine, and supplemented with penicillin (100 U/ml), streptomycin (0.1 mg/ml), and with 10% fetal calf serum (Sigma, Israel). The cells grown at 37°C and 5% CO2. One day before the experiment, cells were resuspended in growing medium (DMEM supplemented with 10% fetal calf serum) $1X10^5$ cells/ml. 50 µL of cell suspension were pipetted into a 96-well plate and grown over night. Thirty minutes before the experiment cells were washed and resuspended in 50 µL of DMEM medium supplemented with L-glutamine (100 U/mL), and with penicillin (100 U/mL), streptomycin (0.1 mg/mL), and with 0.5% heat-inactivated fetal calf serum (assay medium). For the cytotoxicity assay, 100 µM PSMα3 was incubated with or without EGCG at molar ratios of 1:1 or 1:5, or with Poly (AU) RNA at concentrations of 50 ng/µL or 400 ng/µL, for the designated incubation times. Similarly, 100 µM LL-37 was prepared under the same conditions, with or without EGCG at 1:1 or 1:5 molar ratios, or Poly (AU) RNA at 100 ng/µL or 400 ng/µL, following the specified incubation times.

Serial two-fold dilutions in assay medium were performed, and 50 µL of each dilution were pipetted into the three different 96-well with the cells. The plates were incubated for 30 min at 37°C and 5% CO2 and then cell lysis was quantified using the LDH release colorimetric assay according to the manufacturer's instructions, including all recommended controls (LDH; Cytotoxicity Detection Kit Plus, Roche Applied Science, Germany). Cell-free assay medium was measured as background. Cells subjected to the same experimental conditions apart from peptide addition were used as a control to account for spontaneous LDH release. Cells subjected to the same experimental conditions apart from peptide addition and treated with manufacturer-supplied lysis buffer were used as a control to account for maximum LDH release. Absorbance at 490 and 690 nm was measured in a plate reader (FLUOstar Omega, BMG Labtech, Germany). Absorbance at 690 nm was subtracted from 490 nm readings to correct for background. The mean absorbance of triplicate samples and controls was calculated, followed by background subtraction. Data was obtained from at least three independent biological replicates, with the arithmetic mean used for averaging. Error bars represent the standard deviation (SD). Statistical analysis, including one-way ANOVA, was performed using GraphPad Prism 10.

## Assessment of Bacterial Viability Using PrestoBlue™ HS Cell Viability Reagent

*Escherichia coli (E. coli)* cultures were grown overnight in Luria Broth (LB) medium at 37 °C with shaking at 220 rpm. PSMα3 and LL-37 stock solutions were prepared by dissolving the peptides at a concentration of 1 mM in a solvent mixture of 20% DMSO and 80% ultra-pure water. From these

stock solutions, the following sample preparations were made:

For PSMα3: **(1)**100 μM PSMα3 **(2)**100 μM PSMα3 with 50 ng/μL Poly (AU) RNA **(3)** 100 μM PSMα3 with 400 ng/μL Poly (AU) RNA **(4)** 100 μM PSMα3 with 500 μM EGCG. For LL-37: **(1)**100 μM LL-37 **(2)**100 μM LL-37 with 100 ng/μL Poly (AU) RNA **(3)** 100 μM LL-37 with 400 ng/μL Poly (AU) RNA **(4)** 100 μM LL-37 with 500 μM EGCG.

All solutions were prepared in 50 mM HEPES buffer pH 7.4 containing 150 mM NaCl. Where applicable, samples were incubated for the specified durations of 2 hours or 24 hours.

On the day of the experiment, dilutions of the PSMα3 solutions to 20 μM and 10 μM were prepared in LB medium and dispensed into a sterile 96-well black flat-bottom plate (Greiner bio-one). *E. coli* cultures were diluted to an optical density (OD) of 0.2, and bacterial suspensions were added to the wells. The plate was incubated at 37 °C with shaking at 220 rpm for 1 hour to allow the reaction to proceed.

Following incubation, 10X PrestoBlue™ HS Cell Viability Reagent (Invitrogen) was added to the wells. Wells containing only LB medium served as negative controls, while wells containing only *E. coli* served as positive controls. Plates were sealed with a thermal seal film (EXCEL Scientific) and incubated in a plate reader (CLARIOstar). Bacterial viability was assessed using PrestoBlue fluorescence (excitation: 535–560 nm; emission: 590–615 nm) over time. Each condition was tested in triplicate across three independent experiments. Fluorescence values were averaged, and blank readings were subtracted. Antimicrobial activity was determined at the 2-hour time point, when fluorescence was highest in the positive control. Data were obtained from at least three independent biological replicates, with the arithmetic mean used for averaging. Error bars represent the standard deviation (SD). Statistical analysis, including one-way ANOVA, was performed using GraphPad Prism 10.

## Transmission electron microscopy (TEM)

For TEM analysis, 4–5 μL of 100 μM PSMα3, with or without EGCG or Poly(AU) RNA at concentrations of 10 ng/μL, 50 ng/μL, and 400 ng/μL, as well as 100 μM LL-37, with or without Poly(AU) RNA at 100 ng/μL and 400 ng/μL, were directly applied onto glow-discharged 400-mesh copper grids (easiGlow; Pelco, Clovis, CA, USA) with a grid hole size of 42 μm, stabilized with Formvar/carbon (Ted Pella, Inc.). The grids were glow-discharged using a 15-mA current with a negative charge for 25 seconds. Samples were allowed to adhere to the grids for 45 seconds before being stained with a 1% uranyl acetate solution (Electron Microscopy Science, 22400-1) for 45 seconds. The samples were then examined using a ThermoFisher Scientific (FEI) Talos F200C transmission electron microscope, operating at 200 kV and equipped with a Ceta 16M CMOS camera, at the Ilse Katz Institute for Nanoscale Science and Technology, Ben Gurion University of the Negev, Israel.

## Turbidity measurements

Turbidity measurements were performed using a FLUOstar Omega plate reader (BMG Labtech) set to a wavelength of 400 nm. For each sample, the protein concentration was maintained at 100 μM, while RNA concentrations were varied across the following levels: 10 ng/μl, 20 ng/μl, 50 ng/μl, 100 ng /μl, 200 ng/μl, and 400 ng/μl. The turbidity of the mixtures was monitored over several hours following resuspension. The maximum absorbance recorded within the first 30 minutes was used as an indicator of the dense phase volume. The experiments were conducted three times with similar observations.

## Electrophoretic mobility shift assay (EMSA)

RNA molecules were synthesized by IDT, with oligoA modified by the IRDye 800CW fluorescent dye. Double-stranded RNA was prepared by annealing 10 μM oligoA-IRDye 800CW with 10 μM oligoU in an annealing buffer containing 10 mM Tris-HCl (pH 7.5), 50 mM NaCl, and 1 mM EDTA. The mixture was heated to 95°C for 5 minutes, followed by gradual cooling to 25°C at a rate of 2°C per minute. The final RNA concentration used in the binding reactions was 40 nM (~400ng/μL).

RNA-protein complexes were incubated at 37°C for 30 minutes before being resolved on a 2.5% agarose gel. Gel electrophoresis was performed in a 0.5× TBE buffer for 7 minutes. The complexes were visualized using a Li-Cor Odyssey FC imaging system in the 800 nm channel with a 30-second exposure. For the EMSA, binding reactions were carried out in a buffer composed of 20 mM HEPES (pH 7.9), 50 mM KCl, 1 mM Dithiothreitol (DTT), 0.1 mM Ethylenediaminetetraacetic acid (EDTA), 5% glycerol, and 0.05% nonyl phenoxypolyethoxylethanol (NP-40). PSMα3 was added to the reactions at final concentrations of 0, 40, 80, 160, and 320 μM. The experiments were conducted three times with similar observations.

## Fluorescent microscopy imaging of peptides with RNA in vitro

Prior to imaging, 100 μM PSMα3 or LL-37 (containing 20% FITC-labeled and 80% unlabeled peptide) were combined with PI-labeled Poly (AU) RNA at different concentrations in 50 mM HEPES buffer pH 7.4 containing 150 mM NaCl. Sample were also tested after 65°C heat shock for 15 minutes. In addition, the PSMα3 and RNA mixture was also tested in a different buffer containing 20 μM Tris, 20 μM Bis-Tris, and 20 μM sodium acetate at pH 4 and were subjected to heat shock at 65°C for 15 minutes.

Following preparation, with or without heat shock, a 10 μL aliquot of each sample was transferred to a μ-Slide 8 Well ibidi chamber or to a clean 24 × 60 mm No. 1.5 glass slide for imaging. Fluorescence microscopy was performed using a Leica DMI8 inverted fluorescent microscope equipped with a 63× immersion oil objective (Numerical Aperture, NA = 1.4) at the Life Sciences and Engineering (LS&E) Infrastructure Center, Technion-Israel Institute of Technology, Haifa, Israel. Data were processed and analyzed using Fiji-ImageJ software. The experiment was conducted three times with similar observations.

## Fluorescence recovery after photobleaching (FRAP) measurements

FRAP experiments were conducted using a Zeiss LSM 710 laser scanning confocal microscope equipped with a 63× Plan-Apochromat oil immersion objective, NA1.4, at the Life Sciences and Engineering (LS&E) Infrastructure Center, Technion-Israel Institute of Technology, Haifa, Israel. The experiments were performed on condensates from by 100 μM PSMα3-FITC or LL-37-FITC mixed with PI-labeled Poly (AU) RNA at various concentrations as indicated in the figures. Photobleaching was performed using 405 nm and 488 nm laser lines. The experiments were conducted three times with similar observations.

For FRAP analysis inside the nucleolus of HeLa cells, PSMα3 was added to the cells at a final concentration of 20 μM containing 20% FITC-labeled and 80% unlabeled peptide. The cells were incubated with the peptide for 20 minutes before conducting the experiment. Data was processed and analyzed using ZEISS ZEN software and Fiji-ImageJ software. The experiments were conducted three times with similar observations.

## Total internal reflection fluorescence (TIRF) microscopy

TIRF microscopy was performed using a ZEISS Elyra 7 Super-Resolution Microscope equipped with a 63× Apochromat alpha Plan-Apochromat Oil immersion DIC objective, NA1.46, at the Life Sciences and Engineering (LS&E) Infrastructure Center, Technion-Israel Institute of Technology, Haifa, Israel. Images were acquired using the pco.edge sCMOS cameras, and data were processed and analyzed with ZEISS ZEN software to accurately represent the observed phenomena. The condensates and aggregates analyzed were generated using 100 μM PSMα3-FITC with either 50 ng/μL or 400 ng/μL Poly (AU) RNA. AmyTracker 630 (Ebba Biotech) was added at a 1:500 (peptide: AmyTracker) molar ratio to each sample. The experiments were conducted three times with similar observations.

## Confocal microscopy visualization of PSMα3 interaction with HeLa cells

HeLa cells were pre-cultured one day before the experiment by preparing a suspension containing 350,000 cells/ml and plating 150 µl of this suspension into each well of a µ-Slide 8 well glass-bottom chamber. The cells were then incubated overnight under standard growth conditions (37°C, 5% CO2) to allow for adherence and growth. On the day of the experiment, the cells were washed three times with phosphate-buffered saline (PBS) to remove any residual media. Hoechst 33342 dye (10 mg/mL stock) was diluted 1:2000 in fresh cell media and added to the cells. The cells were incubated with Hoechst for 10 minutes at 37°C and 5% CO2. After incubation, cells were washed three times with PBS to remove Hoechst residuals. A working solution of PI was prepared by diluting a 1 mg/ml PI stock solution to a final concentration of 0.02 mg/ml in fresh cell growth media. Immediately prior to imaging, PSMα3 was added to the cells at a final concentration of 20 µM containing 20% FITC-labeled and 80% unlabeled peptide. The cells were then imaged using a Ti2-E microscope by Nikon with a CSU-W1 spinning disk confocal unit by Yokogawa, equipped with a 100X CFI SR HP Plan Apochromat Lambda S silicone immersion objective, NA1.35, at the Life Sciences and Engineering (LS&E) Infrastructure Center, Technion-Israel Institute of Technology, Haifa, Israel. Confocal movies and images were captured by Photometrics BSI sCMOS cameras to observe the interaction and localization of PSMα3 within the cells, focusing particularly on its colocalization with nucleic acids in the nucleolar region. The acquired images and movies were subsequently analyzed using Imaris Image Analysis Software (Oxford Instruments). The experiments were conducted three times with similar observations.

## Super resolution light microscopy visualization of PSMα3 interaction with *E. coli*

*E. coli* lptD4213 cells were a kind gift from Prof. Sima Yaron from the Technion – Israel Institute of Technology. An inoculum was pre-cultured in Luria-Bertani medium (LB) medium at 220 rpm and 37°C for 24 hours prior to the experiment. On the day of the experiment, the optical density (OD) of the culture was measured, and the cells were diluted to an OD of 0.4. The cells were then incubated with 20 µM PSMα3, with and without EGCG at 1:5 molar ratio, alongside a bacteria-only control. Samples were incubated for 30 minutes at 220 rpm and 37°C. Following incubation, the samples were centrifuged three times for 3 minutes at 1.5g, with the supernatant discarded and the pellet resuspended in 1X PBS after each spin. The resuspended cells were then stained with 50 µg/mL wheat germ agglutinin (WGA) CF633 for 30 minutes. After staining, the cells were washed three times by centrifugation with PBS to remove excess WGA. During the final wash, the cells were resuspended in 0.1 mg/mL PI solution.

Prior to imaging, the samples were loaded into an ibidi µ-Slide VI 0.4. Imaging was performed using a ZEISS Elyra 7 Super-Resolution Microscope equipped with a 63× Apochromat alpha Plan-Apochromat Oil immersion DIC objective, NA 1.4, and pco.edge sCMOS cameras. Lattice structured illumination images were acquired and processed using the ZEN black software at the Life Sciences and Engineering (LS&E) Infrastructure Center, Technion-Israel Institute of Technology, Haifa, Israel. The experiments were conducted three times with similar observations.

## Thioflavin T fluorescence fibrillation kinetics assay

Thioflavin T (ThT) (Sigma Aldrich) is a widely used fluorescent dye for detecting and analyzing amyloid fibril formation kinetics. Fibrillation curves in the presence of ThT typically exhibit an initial lag phase followed by rapid fibril elongation. To accurately capture the fibrillation lag time, PSMα3 was pre-treated before the experiment. The peptide was dissolved in a 1:1 mixture of 1,1,1,3,3,3-Hexafluoroisopropanol (HFIP-Sigma Aldrich) and Trifluoroacetic acid (TFA-Sigma Aldrich) to a final concentration of 1 mg/mL, followed by bath sonication for 10 minutes at room temperature. The organic solvents were then evaporated using a mini-rotational vacuum concentrator (Christ, Germany) at 1,000 rpm for 2 hours at room temperature.

For the experiment, freshly prepared 100 μM PSMα3 peptides, with or without 500 μM Epigallocatechin gallate (EGCG) at a 1:5 molar ratio, were prepared in 50 mM HEPES buffer pH 7.4 containing 150 mM NaCl. ThT was prepared by diluting a stock solution in ultrapure double-distilled water (UPddw) and filtered before use to reach a final concentration of 200 μM Blank control solutions containing all components except for the peptide were prepared for each reaction.

The assay was conducted in black 96-well flat-bottom plates (Greiner Bio-One), which were sealed with a thermal seal film (EXCEL Scientific) to prevent evaporation. Samples were incubated in a plate reader (OMEGA) at 37°C, shaking at 500 rpm for 85 seconds before each reading cycle, for up to 1,000 cycles of 6 minutes each, totaling approximately 100 hours. Fluorescence was measured in triplicate using an excitation wavelength of 438 ± 20 nm and an emission wavelength of 490 ± 20 nm. All values were averaged, background fluorescence was subtracted using blank controls, and the results were plotted over time. Standard error of the mean is shown as error bars. The entire experiment was independently repeated at least three times on different days to ensure reproducibility.

## Solid-State Circular Dichroism Spectroscopy

Solid-state circular dichroism spectroscopy(ss-CD) was conducted with PSMa3 to assess their fibrillar secondary structure components in presence and absence of Poly (AU) RNA. For preparation of peptide and RNA samples, see Peptide and Poly (AU) preparation section. PSMa3 was prepared at a working concentration of 100 μM in 50 mM HEPES, pH 7.4, 150 mM NaCl at 0 ng/μL, 50 ng/μL or 400 ng/μL Poly (AU) RNA. The reaction mixes were incubated for 0 min, 2 h and 72 h at 37 °C in a non-shaking thermocycler. Following incubation, soluble reaction components were removed via dilution washing with 150 μL water and centrifugation at 12.500 rcf for 30 min. 20 μL of the sediment were resuspended in 180 μL water for a second washing centrifugation step at 12.500 rcf for 30 min. 180 μL of the supernatant were discarded and 18 μL of sediment applied to a *Chirascan Series fused silica disc* (AP/CSSD, Applied Photophysics) in three times 6 μL steps. After every sample application onto to the silica disc, all liquid was evaporated at 37 °C for 5–10 min until only an opaque film remained visible. For secondary structure determination of aggregated/fibrillar peptide components on the silica disc, the disc was inserted into a *Chirascan solid sample holder* (CS/SSH, Applied Photophysics) and the circular dichroism recorded in the far-UV (180–250 nm, step size 1 nm, time-per-point 1 s) using a CD spectropolarimeter (Applied Photophysics). To counteract sample anisotropy, CD spectra were recorded at least four different disc rotations and the results averaged. Prior to data analysis, silica disc and buffer/water backgrounds were subtracted from recorded sample spectra. Poly (AU) RNA-only background spectra showed complex and high amplitude signals that did not appear for samples in combination with peptides and were therefore not subtracted from sample spectra.

## NMR experiments

To prepare the reference samples for NMR analysis, 0.521 mg of PSMα3 was dissolved in 180 μL of 20 mM MES (2-(N-morpholino)ethanesulfonic acid) buffer at pH 6.0, supplemented with 5% (v/v) deuterium oxide ($D_2O$). From this solution, 170 μL was transferred into a 3.0 mm NMR tube for spectral acquisition. In parallel, a 4 mM stock solution of EGCG was prepared in the same 20 mM MES buffer (pH 6.0). From this, a working solution containing 0.5 mM EGCG in 20 mM MES with 5% (v/v) $D_2O$ was prepared to match the buffer conditions of the peptide sample. A volume of 170 μL was then transferred into a separate 3.0 mm NMR tube for use as the EGCG reference.

All NMR experiments were recorded on a Bruker 700 MHz spectrometer equipped with a triple-resonance cryoprobe (Prodigy) and an AVANCE NEO console. One-dimensional (1D) $^1$H-NMR spectra were acquired using the Bruker library pulse sequence zggpw5 for water suppression. The acquisition parameters were: acquisition time (AQ) = 1.90 s, spectral width (SW) = 12.31 ppm, recovery delay (D1) = 1.5 s, and 64 scans. All experiments were conducted at 35 °C, under which optimal spectral quality was obtained.

Two-dimensional (2D) $^1H$–$^1H$ TOCSY (Total Correlation Spectroscopy) spectra were collected using the Bruker pulse sequence dipsi2gpph19. Acquisition parameters were: $t_2$ = 2048 complex points ($AQ_2$ = 0.118 s), $t_1$ = 512 complex points ($AQ_1$ = 0.029 s), $SW_1 = SW_2$ = 12.31 ppm, with 64 scans and a mixing time (tmix) of 80 ms. Recovery delay (D1) was set to 1.5 s. 2D $^1H$–$^1H$ NOESY (Nuclear Overhauser Effect Spectroscopy) spectra were acquired using the noesyfpgpph19 pulse sequence, with acquisition parameters identical to those used for TOCSY. The mixing time was set to 300 ms. Total experimental time for the combined 2D TOCSY and NOESY experiments was approximately 30 hours. NMR data processing was carried out using TopSpin 4.5.0 (Bruker), and spectral assignments for the 2D TOCSY and NOESY spectra were performed using POKY software[68]. Signal integration was carried out using in-house scripts written in Scilab[69].

# Supplementary Information

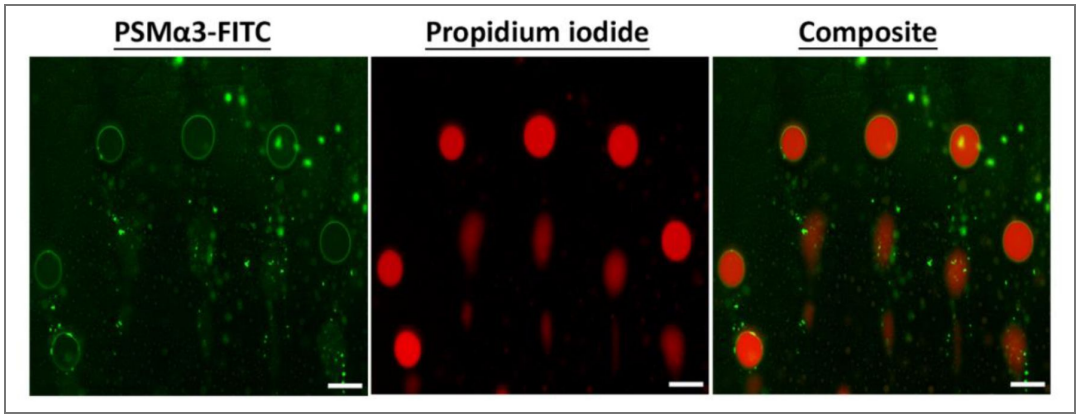


**Figure S1. Encapsulation of Poly (AU) RNA within PSMα3-FITC droplets.** FITC-PSMα3 (green) was mixed with 50 ng/μL Poly (AU) RNA labeled with PI. The left panel shows the FITC green channel, the middle panel displays the PI red channel, and the right panel is a composite image showing the overlap of PSMα3-FITC and Poly (AU) RNA-PI signals. Scale bars represent 20 μm.

**Figure S2. Turbidity measurements of PSMα3 with increasing Poly (AU) RNA concentrations.**

PSMα3 concentration was maintained at 100 μM, and Poly (AU) RNA concentrations varied across 0, 10, 20, 50, 100, 200, and 400 ng/μL. Data points represent the average optical density at 400 nm (OD400) recorded within the first 30 minutes post-resuspension, with each condition tested in triplicate. Error bars indicate the standard error of the mean.

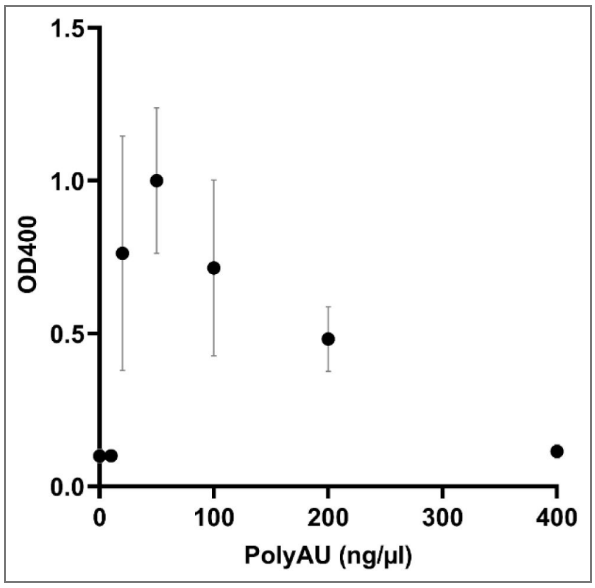


**Figure S3. RNA stabilizes an α-helical conformation of PSMα3 over time.**

Solid-state circular dichroism (ssCD) spectra of PSMα3 incubated alone or with polyAU RNA at concentrations of 50 ng/μL and 400 ng/μL. Spectra were collected immediately after preparation (**A**), and after 2 hours of incubation (**B**). Measurements were recorded in the far-UV range (180–250 nm) to assess changes in secondary structure under the indicated conditions.

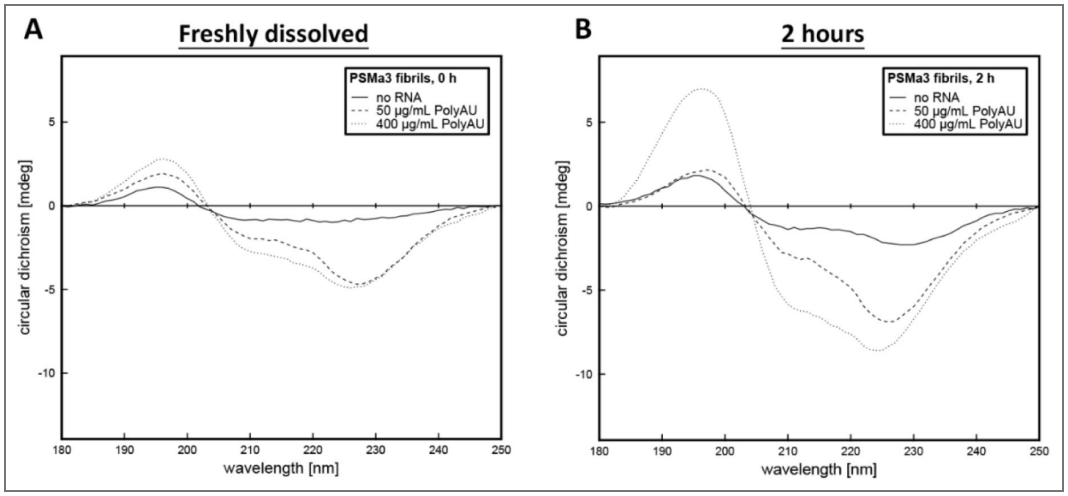

**Figure S4. EGCG inhibits PSMα3 Fibrillation.**

Fibrillation kinetics of 100 μM freshly dissolved PSMα3, monitored by Thioflavin-T (ThT) fluorescence. The data compares PSMα3 fibrillation in the absence (blue curve) and presence (red curve) of EGCG. The graph displays the mean fluorescence intensities from triplicate ThT measurements, with error bars representing the standard error of the mean.

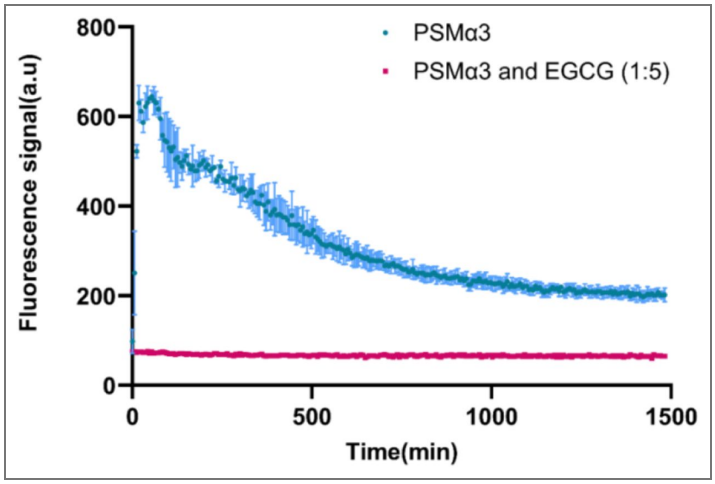


**Figure S5. EGCG reduces the antimicrobial activity of PSMα3 against *E. coli*.**

**(A)** Super-resolution light microscopy images of E. coli treated with 20 μM PSMα3-FITC (green) in the absence (left) and presence (right) of EGCG at a 1:5 molar ratio. Scale bars: 5 μm. **(B)** Antimicrobial activity of PSMα3 against E. coli, evaluated using the PrestoBlue cell viability assay, with and without EGCG (1:5 molar ratio). The experiments were performed in at least three replicates and repeated across three independent days to ensure result reliability. Cytotoxicity and bacterial cell viability percentages were calculated as the mean of all replicates, with error bars representing the standard error of the mean (SEM). Statistical significance was determined using one-way ANOVA for normally distributed data in GraphPad Prism (version 11). Significance levels are indicated as follows: *p<0.05, **p<0.01, ***p<0.001, ****p<0.0001.

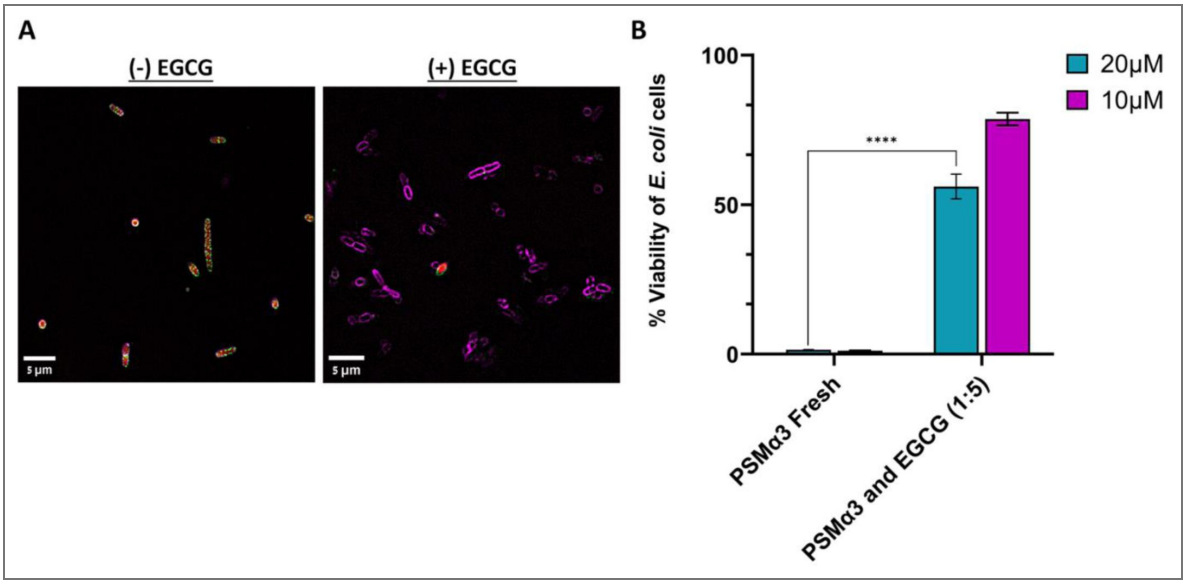

**Figure S6.** **LL37 undergoes aggregation with Poly (AU) RNA before heat shock.**

Light microscopy images showing LL37-FITC (green) forming aggregates in the presence of 100 ng/μL Poly (AU) RNA, stained with propidium iodide (red). The composite image (right) highlights the colocalization of LL37 and RNA (yellow), indicating RNA-induced aggregation. Scale bars: 20 μm.

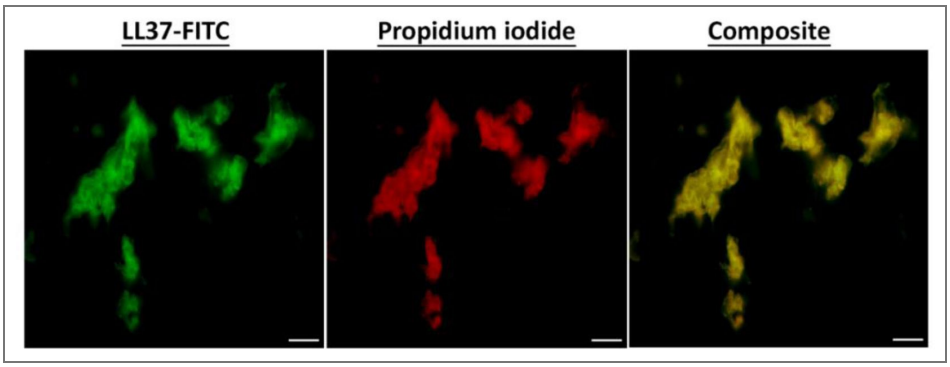


**Figure S7.** **PSMα3 aggregates with Poly (AU) RNA after heat shock at physiological pH.**

Light microscopy images showing PSMα3-FITC (green) forming aggregates with 50 ng/μL Poly (AU) RNA, stained with propidium iodide (red), after heat shock at 60°C for 15 minutes in 50 mM HEPES, 150 mM NaCl, at physiological pH (7.4). The composite image (right) highlights the colocalization of PSMα3 and RNA (yellow), indicating RNA-induced aggregation under heat stress. Scale bars: 20 μm.

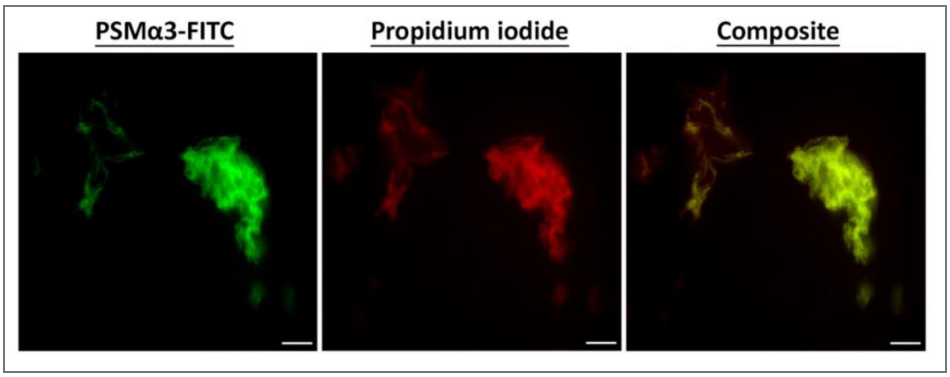

**Figure S8. Effect of RNA concentration on PSMα3 phase separation and aggregation at pH 4 after heat shock.**

Fluorescence microscopy images showing the effects on PSMα3-FITC (green) in the presence of increasing concentrations of Poly (AU) RNA (labeled with Propidium Iodide, red) following heat shock at 65°C for 15 minutes at pH 4. at 50 ng/μL (**A**), 100 ng/μL (**B**), 200 ng/μL (**C**) and 400 ng/μL (**D**). At a low RNA concentration of 50 ng/μL (**A**), clear phase separation of PSMα3 was observed, as evidenced by the presence of well-defined, spherical droplets. As the RNA concentration increased to 100 ng/μL, the droplets began to lose their spherical structure and showed more morphological irregularities (**B**). At RNA concentrations of 200 ng/μL and 400 ng/μL, a distinct transition to aggregation with irregular, amorphous clusters were observed (**C** and **D**, respectively). The composite images revealed an overlap between the PSMα3 and RNA, indicating co-localization during both phase separation and amorphous cluster formation. Scale bars in all images represent 20 μm.

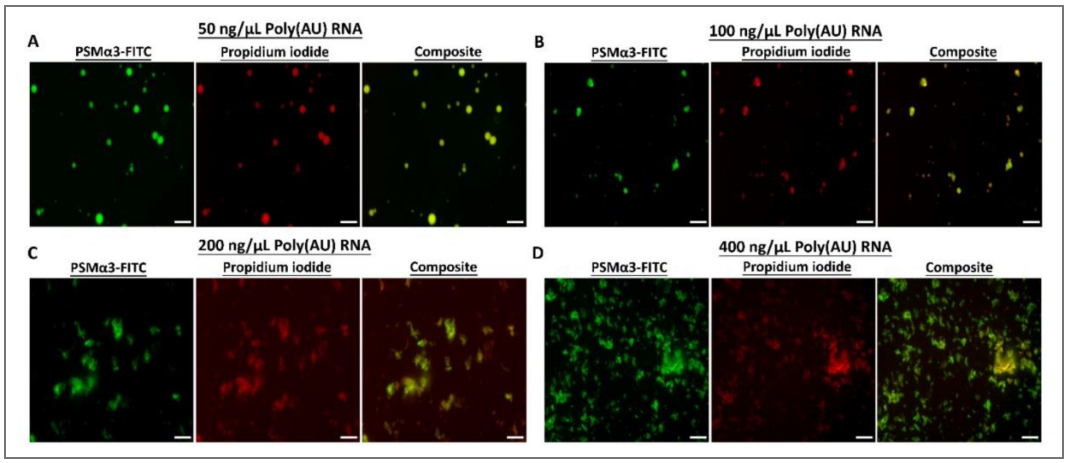


**Figure S9. Poly (AU) RNA Modulates LL-37 Aggregation Dynamics Before and After Heat Shock.**

TEM micrographs of 100 μM LL-37 incubated alone or with 100 ng/μL or 400 ng/μL Poly (AU) RNA for 2 hours or 24 hours. **(A)** Samples imaged before heat shock at the indicated point. **(B)** Samples subjected to a 65°C heat shock for 15 minutes, followed by further incubation for 2 or 24 hours before imaging.

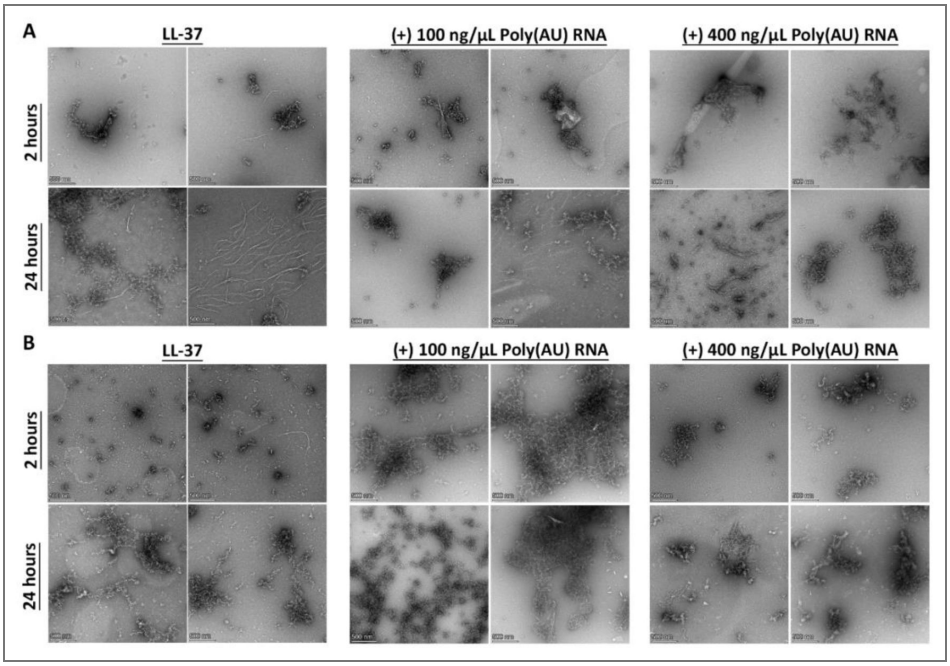

## Data availability

The data is available at *https://zenodo.org/records/17116616* and upon request

## Acknowledgements

M.L. acknowledges research support from the Israel Science Foundation, Grant No. 2111/20 and the Cure Alzheimer's Fund. M.L. and M.Z. acknowledge the Forschungskooperation Niedersachsen – Israel, Volkswagenstiftung, No: 76251-4659/2022 (ZN 4042). Funded/Co-funded by the European Union (ERC, FuncAmyloid, 101087140). Views and opinions expressed are however those of the author(s) only and do not necessarily reflect those of the European Union or the European Research Council. Neither the European Union nor the granting authority can be held responsible for them. A.K.B thanks the Novo Nordisk Foundation (Grant number NNFSA17002839) and the European Union (ERC CoG 101088163 EMMA) for funding. We thank Ayala Shiber for advice and guidance, as well as Yael Mandel-Gutfreund and Hiba Hassanain for their assistance with RNA preparations. We acknowledge guidance and support from Nitsan Dahan from the Microscopy core facility center at the Lorry I. Lokey Interdisciplinary Center for Life Sciences and Engineering. We acknowledge the use of OpenAI's GPT-4 model to improve the writing quality of parts of this manuscript.

## Additional information

### Funding


| Funder | Grant reference number |
|---|---|
| Israel Science Foundation | 2111/20 |
| Cure Alzheimer's Fund | |
| Volkswagen Foundation | 76251-4659/2022 (ZN 4042) |
| European Research Council | https://doi.org/10.3030/101087140 |
| European Research Council | https://doi.org/10.3030/101088163 |
| Novo Nordisk Foundation | NNFSA17002839 |


### Author ORCID iDs

**Alexander K Buell**: https://orcid.org/0000-0003-1161-3622
**Meytal Landau**: https://orcid.org/0000-0002-1743-3430

## References

1. **Zaman M.,** Andreasen M (2020) Cross-talk between individual phenol-soluble modulins in Staphylococcus aureus biofilm enables rapid and efficient amyloid formation. *eLife* **9**:e59776 https://doi.org/10.7554/eLife.59776
2. **Barnhart M. M.,** Chapman M. R. (2006) Curli biogenesis and function. *Annu Rev Microbiol* **60**:131-147
3. **Rayan B.,** Barnea E., Khokhlov A., Upcher A., Landau M (2023) Differential fibril morphologies and thermostability determine functional roles of Staphylococcus aureus PSMα1 and PSMα3. *Front Mol Biosci* **10**
4. **Marinelli P.,** Pallares I., Navarro S., Ventura S (2016) Dissecting the contribution of Staphylococcus aureus α-phenol-soluble modulins to biofilm amyloid structure. *Sci Rep* **6**:34552

5. **Schwartz K.,** Syed A. K., Stephenson R. E., Rickard A. H., Boles B. R (2012) Functional amyloids composed of phenol soluble modulins stabilize Staphylococcus aureus biofilms. *PLoS Pathog* **8**:e1002744
6. **Sleutel M.,** Pradhan B., Volkov A. N., Remaut H (2023) Structural analysis and architectural principles of the bacterial amyloid curli. *Nat Commun* **14**:2822
7. **Perov S.,** et al. (2019) Structural Insights into Curli CsgA Cross-β Fibril Architecture Inspire Repurposing of Anti-amyloid Compounds as Anti-biofilm Agents. *PLoS Pathog* **15**:e1007978
8. **Howard M. K.,** et al. (2023) Probing the drivers of Staphylococcus aureus biofilm protein amyloidogenesis and disrupting biofilms with engineered protein disaggregases. *mBio* **14**:e00587-23
9. **Chapman M. R.,** et al. (2002) Role of Escherichia coli curli operons in directing amyloid fiber formation. *Science* **295**:851-855
10. **Blanco L. P.,** Evans M. L., Smith D. R., Badtke M. P., Chapman M. R (2012) Diversity, biogenesis and function of microbial amyloids. *Trends Microbiol* **20**:66-73
11. **Le K. Y.,** Dastgheyb S., Ho T. V., Otto M (2014) Molecular determinants of staphylococcal biofilm dispersal and structuring. *Front Cell Infect Microbiol* **4**
12. **Peschel A.,** Otto M. (2013) Phenol-soluble modulins and staphylococcal infection. *Nat Rev Microbiol* **11**:667-673
13. **Mehlin C.,** Headley C. M., Klebanoff S. J (1999) An Inflammatory Polypeptide Complex from Staphylococcus epidermidis: Isolation and Characterization. *J Exp Med* **189**:907-918
14. **Chatterjee S. S.,** et al. (2013) Essential Staphylococcus aureus toxin export system. *Nat Med* **19**:364-367
15. **Kretschmer D.,** et al. (2010) Human formyl peptide receptor 2 senses highly pathogenic Staphylococcus aureus. *Cell Host Microbe* **7**:463-473
16. **Queck S. Y.,** et al. (2009) Mobile Genetic Element-Encoded Cytolysin Connects Virulence to Methicillin Resistance in MRSA. *PLoS Pathog* **5**:e1000533
17. **Joo H.-S.,** Otto M (2012) Molecular basis of in vivo biofilm formation by bacterial pathogens. *Chem Biol* **19**:1503-1513
18. **Hu Z.,** et al. (2022) Phenol-soluble modulin α and β display divergent roles in mice with staphylococcal septic arthritis. *Commun Biol* **5**:1-11
19. **Grando K.,** et al. (2022) Phenol-Soluble Modulins From Staphylococcus aureus Biofilms Form Complexes With DNA to Drive Autoimmunity. *Front Cell Infect Microbiol* **12**
20. **Cheung G. Y. C.,** Joo H.-S., Chatterjee S. S., Otto M (2014) Phenol-soluble modulins--critical determinants of staphylococcal virulence. *FEMS Microbiol Rev* **38**:698-719
21. **Schwartz K.,** et al. (2014) The AgrD N-terminal leader peptide of Staphylococcus aureus has cytolytic and amyloidogenic properties. *Infect Immun* **82**:3837-3844
22. **Tayeb-Fligelman E.,** Salinas N., Tabachnikov O., Landau M (2020) Staphylococcus aureus PSMα3 Cross-α Fibril Polymorphism and Determinants of Cytotoxicity. *Structure* **28**:301-313.e6
23. **Tayeb-Fligelman E.,** et al. (2017) The cytotoxic Staphylococcus aureus PSMα3 reveals a cross-α amyloid-like fibril. *Science* **355**:831-833
24. **Kreutzberger M. A. B.,** et al. (2022) Phenol-soluble modulins PSMα3 and PSMβ2 form nanotubes that are cross-α amyloids. *Proc Natl Acad Sci U S A* **119**:e2121586119
25. **Schwartz K.,** Boles B. R (2013) Microbial amyloids--functions and interactions within the host. *Curr Opin Microbiol* **16**:93-99
26. **Malishev R.,** et al. (2018) Reciprocal Interactions between Membrane Bilayers and S. aureus PSMα3 Cross-α Amyloid Fibrils Account for Species-Specific Cytotoxicity. *J Mol Biol* **430**:1431-1441
27. **Sancho-Vaello E.,** et al. (2020) The structure of the antimicrobial human cathelicidin LL-37 shows oligomerization and channel formation in the presence of membrane mimics. *Sci Rep* **10**

28. **Engelberg Y.,** Landau M (2020) The Human LL-37(17-29) antimicrobial peptide reveals a functional supramolecular structure. *Nat Commun* **11**:3894
29. **Rumpret M.,** et al. (2021) Signal inhibitory receptor on leukocytes-1 recognizes bacterial and endogenous amphipathic α-helical peptides. *FASEB J* **35**:e21875
30. **Golan N.,** Engelberg Y., Landau M (2022) Structural Mimicry in Microbial and Antimicrobial Amyloids. *Annual Review of Biochemistry* **91**:403-422
31. **Rautenberg M.,** Joo H.-S., Otto M., Peschel A (2011) Neutrophil responses to staphylococcal pathogens and commensals via the formyl peptide receptor 2 relates to phenol-soluble modulin release and virulence. *FASEB J* **25**:1254-1263
32. **Syed A. K.,** Reed T. J., Clark K. L., Boles B. R., Kahlenberg J. M (2015) Staphlyococcus aureus phenol-soluble modulins stimulate the release of proinflammatory cytokines from keratinocytes and are required for induction of skin inflammation. *Infect Immun* **83**:3428-3437
33. **Schreiner J.,** et al. (2013) Staphylococcus aureus phenol-soluble modulin peptides modulate dendritic cell functions and increase in vitro priming of regulatory T cells. *J Immunol* **190**:3417-3426
34. **Chu M.,** et al. (2018) Staphylococcus aureus Phenol-Soluble Modulins α1-α3 Act as Novel Toll-Like Receptor (TLR) 4 Antagonists to Inhibit HMGB1/TLR4/NF-κB Signaling Pathway. *Front Immunol* **9**
35. **Kretschmer D.,** Nikola N., Dürr M., Otto M., Peschel A (2012) The Virulence Regulator Agr Controls the Staphylococcal Capacity to Activate Human Neutrophils via the Formyl Peptide Receptor 2. *J Innate Immun* **4**:201-212
36. **Bröker B. M.,** Mrochen D., Péton V (2016) The T Cell Response to Staphylococcus aureus. *Pathogens* **5**
37. **Ganguly D.,** et al. (2009) Self-RNA-antimicrobial peptide complexes activate human dendritic cells through TLR7 and TLR8. *J Exp Med* **206**:1983-1994
38. **Tewary P.,** et al. (2013) β-Defensin 2 and 3 promote the uptake of self or CpG DNA, enhance IFN-α production by human plasmacytoid dendritic cells, and promote inflammation. *J Immunol* **191**:865-874
39. **Schmidt N. W.,** et al. (2015) Liquid-crystalline ordering of antimicrobial peptide-DNA complexes controls TLR9 activation. *Nat Mater* **14**:696-700
40. **Lee E. Y.,** et al. (2019) Helical antimicrobial peptides assemble into protofibril scaffolds that present ordered dsDNA to TLR9. *Nat Commun* **10**:1012
41. **Grando K.,** et al. (2022) Phenol-Soluble Modulins From Staphylococcus aureus Biofilms Form Complexes With DNA to Drive Autoimmunity. *Front Cell Infect Microbiol* **12**:884065
42. **Gallo P. M.,** et al. (2015) Amyloid-DNA Composites of Bacterial Biofilms Stimulate Autoimmunity. *Immunity* **42**:1171-1184
43. **Tursi S. A.,** et al. (2017) Bacterial amyloid curli acts as a carrier for DNA to elicit an autoimmune response via TLR2 and TLR9. *PLOS Pathogens* **13**:e1006315
44. **Alberti S.,** Gladfelter A., Mittag T (2019) Considerations and Challenges in Studying Liquid-Liquid Phase Separation and Biomolecular Condensates. *Cell* **176**:419-434
45. **Hyman A. A.,** Weber C. A., Jülicher F. (2014) Liquid-liquid phase separation in biology. *Annual review of cell and developmental biology* **30**
46. **Wang B.,** et al. (2021) Liquid-liquid phase separation in human health and diseases. *Signal transduction and targeted therapy* **6**
47. **Xu Z.,** Wang W., Cao Y., Xue B (2023) Liquid-liquid phase separation: Fundamental physical principles, biological implications, and applications in supramolecular materials engineering. *Supramolecular Materials* **2**
48. **Indig R. Y.,** Landau M (2023) Designed inhibitors to reduce amyloid virulence and cytotoxicity and combat neurodegenerative and infectious diseases. *Current Opinion in Chemical Biology* **75**:102318
49. **Fernandes L.,** Cardim-Pires T. R., Foguel D., Palhano F. L (2021) Green Tea Polyphenol Epigallocatechin-Gallate in Amyloid Aggregation and Neurodegenerative Diseases. *Front Neurosci* **15**:718188

50. **Andrich K.,** Bieschke J (2015) The Effect of (-)-Epigallo-catechin-(3)-gallate on Amyloidogenic Proteins Suggests a Common Mechanism. *Adv Exp Med Biol* **863**:139-161
51. **Nott T. J.,** et al. (2015) Phase Transition of a Disordered Nuage Protein Generates Environmentally Responsive Membraneless Organelles. *Mol Cell* **57**:936-947
52. **Sternke-Hoffmann R.,** Peduzzo A., Bolakhrif N., Haas R., Buell A. K (2020) The Aggregation Conditions Define Whether EGCG is an Inhibitor or Enhancer of α-Synuclein Amyloid Fibril Formation. *Int J Mol Sci* **21**:1995
53. **Riback J. A.,** et al. (2017) Stress-Triggered Phase Separation Is an Adaptive, Evolutionarily Tuned Response. *Cell* **168**:1028-1040.e19
54. **De Lorenzi E.,** et al. (2017) Evidence that the Human Innate Immune Peptide LL-37 may be a Binding Partner of Amyloid-β and Inhibitor of Fibril Assembly. *J Alzheimers Dis* **59**:1213-1226
55. **Murakami T.,** et al. (2015) ALS/FTD Mutation-Induced Phase Transition of FUS Liquid Droplets and Reversible Hydrogels into Irreversible Hydrogels Impairs RNP Granule Function. *Neuron* **88**:678-690
56. **Wang Y.-L.,** et al. (2023) Liquid-liquid phase separation in DNA double-strand breaks repair. *Cell Death Dis* **14**:1-10
57. **Kanaan N. M.,** Hamel C., Grabinski T., Combs B (2020) Liquid-liquid phase separation induces pathogenic tau conformations in vitro. *Nat Commun* **11**:2809
58. **Ambadipudi S.,** Biernat J., Riedel D., Mandelkow E., Zweckstetter M (2017) Liquid– liquid phase separation of the microtubule-binding repeats of the Alzheimer-related protein Tau. *Nat Commun* **8**
59. **Boyko S.,** Surewicz W. K (2022) Tau liquid–liquid phase separation in neurodegenerative diseases. *Trends in Cell Biology* **32**:611-623
60. **Wegmann S.,** et al. (2018) Tau protein liquid–liquid phase separation can initiate tau aggregation. *The EMBO Journal* https://doi.org/10.15252/embj.201798049
61. **Babinchak W. M.,** et al. (2019) The role of liquid–liquid phase separation in aggregation of the TDP-43 low-complexity domain. *Journal of Biological Chemistry* **294**:6306-6317
62. **Mukherjee S.,** Poudyal M., Dave K., Kadu P., Maji S. K (2024) Protein misfolding and amyloid nucleation through liquid–liquid phase separation. *Chem. Soc. Rev* **53**:4976-5013
63. **Ray S.,** et al. (2020) α-Synuclein aggregation nucleates through liquid–liquid phase separation. *Nat. Chem* **12**:705-716
64. **Patel A.,** et al. (2015) A Liquid-to-Solid Phase Transition of the ALS Protein FUS Accelerated by Disease Mutation. *Cell* **162**:1066-1077
65. **Röntgen A.,** et al. (2025) Aggregation of α-synuclein splice isoforms through a phase separation pathway. *Sci Adv* **11**:eadq5396
66. **Elbaum-Garfinkle S** (2019) Matter over mind: Liquid phase separation and neurodegeneration. *J Biol Chem* **294**:7160-7168
67. **Sneideris T.,** et al. (2023) Targeting nucleic acid phase transitions as a mechanism of action for antimicrobial peptides. *Nat Commun* **14**:7170
68. **Lee W.,** Rahimi M., Lee Y., Chiu A (2021) POKY: a software suite for multidimensional NMR and 3D structure calculation of biomolecules. *Bioinformatics* **37**:3041-3042
69. **Campbell S. L.,** Chancelier J.-P., Nikoukhah R (2010) Modeling and Simulation in Scilab. In: *Modeling and Simulation in Scilab/Scicos with ScicosLab 4.4* New York, NY: Springer. pp. 73-106 https://doi.org/10.1007/978-1-4419-5527-2_3

# Peer reviews

## Reviewer #1 (Public review):

Summary:

The manuscript by Rayan et al. aims to elucidate the role of RNA as a context-dependent modulator of liquid-liquid phase separation (LLPS), aggregation, and bioactivity of the amyloidogenic peptides PSMα3 and LL-37, motivated by their structural and functional similarities.

Strengths:

The authors combine extensive biophysical characterization with cell-based assays to investigate how RNA differentially regulates peptide aggregation states and associated cytotoxic and antimicrobial functions.

Weaknesses:

While the study addresses an interesting and timely question with potentially broad implications for host-pathogen interactions and amyloid biology, several aspects of the experimental design and data analysis require further clarification and strengthening.

Major Comments:

(1) In Figure 1A, the author showed "stronger binding affinity" based on shifts at lower peptide concentrations, but no quantitative binding parameters (e.g., apparent Kd, fraction bound, or densitometric analysis) are presented. This claim would be better supported by including: (i) A binding curve with quantification of free vs bound RNA band intensities (ii) Replicates and error estimates (mean {plus minus} SD).

(2) The authors report droplet formation at low RNA (50 ng/μL) but protein aggregation at high RNA (400 ng/μL) through fluorescence microscopy. However, no intermediate RNA concentrations (e.g., 100-300 ng/μL) are tested or discussed, leaving a critical gap in understanding the full phase diagram and transition mechanisms. Additionally, the behaviour of PSMα3 in the absence of RNA under LLPS conditions is not shown. Without protein-only data, it is difficult to assess if droplets are RNA-induced or if protein has a weak baseline LLPS that RNA tunes. The saturation concentration (csat) for PSMα3 phase separation, either in the absence or presence of RNA, should be reported.

(3) For a convincing LLPS claim, it is important to show: Quantitative FRAP curves (mobile fraction and half-time of recovery) rather than only microscopy images and qualitative statements.

(4) The manuscript highly relies on fluorescence microscopy to show colocalization. However, the colocalization is presented in a qualitative manner only. The manuscript would benefit from the inclusion of quantitative metrics (e.g., Pearson's correlation coefficient, Manders' overlap coefficients, or intensity correlation analysis).

(5) In Figures 3 B and 3C, the contrast between "no AT630 at 30 min, strong at 2 h" (50 ng/μL) and "strong at 30 min" (400 ng/μL) is compelling, but a simple quantification (e.g., mean fluorescence intensity per area) would greatly increase rigor.

(6) In Figure S3 ssCD data, if possible, indicate whether the α-helical signal increases with RNA concentration or shows a non-linear dependence, which might link to the LLPS vs solid aggregate regimes.

(7) In Figure 5B, FRAP recovery in dying cells may reflect artifactual mobility rather than biological relevance. Additionally, the absence of quantification data limits interpretation; providing recovery curves would clarify relevance.

(8) The narrative conflates cytotoxicity endpoints (membrane damage, PI staining, aggregates) with localization data (nucleolar foci), creating ambiguity about whether

nucleolar targeting drives toxicity or is a consequence of cell death. Separating toxicity assessment from localization analysis, or clearly demonstrating that nucleolar accumulation precedes cytotoxicity, would resolve this ambiguity.

(9) In Figure 8, to strengthen the LLPS assignment for LL-37, additional evidence, such as FRAP analysis or observation of droplet fusion events, would be valuable. This is particularly relevant given that the heat shock conditions (65{degree sign}C for 15 minutes) could potentially induce partial denaturation or nonspecific coacervation.

https://doi.org/10.7554/eLife.109290.1.sa3

## Reviewer #2 (Public review):

In this paper, Rayan et al. report that RNA influences cytotoxic activity of the staphylococcal secreted peptide cytolysin PSMalpha3 versus human cells and E. coli by impacting its aggregation. The authors used sophisticated methods of structural analysis and described the associated liquid-liquid phase separation. They also compare the influence of RNA on the aggregation and activity of LL-37, which shows differences from that on PSMalpha3.

Strengths:

That RNA impacts PSM cytotoxicity when co-incubated in vitro becomes clear.

Weaknesses:

I have two major and fundamental problems with this study:

(1) The premise, as stated in the introduction and elsewhere, that PSMalpha3 amyloids are biologically functional, is highly debatable and has never been conclusively substantiated. The property that matters most for the present study, cytotoxicity, is generally attributed to PSM monomers, not amyloids. The likely erroneous notion that PSM amyloids are the predominant cytotoxic form is derived from an earlier study by the authors that has described a specific amyloid structure of aggregated PSMalpha3. Other authors have later produced evidence that, quite unsurprisingly, indicated that aggregation into amyloids decreases, rather than increases, PSM cytotoxicity. Unfortunately, yet other groups have, in the meantime, published in-vitro studies on "functional amyloids" by PSMs without critically challenging the concept of PSM amyloid "functionality". Of note, the authors' own data in the present study, which show strongly decreased cytotoxicity of PSMalpha3 after prolonged incubation, are in agreement with monomer-associated cytotoxicity as they can be easily explained by the removal of biologically active monomers from the solution.

(2) That RNA may interfere with PSM aggregation and influence activity is not very surprising, given that PSM attachment to nucleic acids - while not studied in as much detail as here - has been described. Importantly, it does not become clear whether this effect has biologically significant consequences beyond influencing, again not surprisingly, cytotoxicity in vitro. The authors do show in nice microscopic analyses that labeled PSMalpha3 attaches to nuclei when incubated with HeLa cells. However, given that the cells are killed rapidly by membrane perturbation by the applied PSM concentrations, it remains unclear and untested whether the attachment to nucleic acids in dying cells makes any contribution to PSM-induced cell death or has any other biological significance.

Overall, the findings can be explained in a much more straightforward way with the common concept of cytotoxicity being due to monomeric PSMs, and the impact of nucleic acids on cytotoxicity being due to lowering of the concentration of that active form by RNA attachment. Further limiting the significance of the findings, whether this interaction has any biological significance on the physiology or infectivity of the PSM producer remains largely unexplored.

https://doi.org/10.7554/eLife.109290.1.sa2

## Reviewer #3 (Public review):

Summary:

The manuscript by Rayan et al. aims to investigate the role of RNA in modulating both virulent amyloid and host-defense peptides, with the objective of understanding their self-assembly mechanisms, morphological features, and aggregation pathways.

Strengths:

The overall content is well-structured with a logical flow of ideas that effectively conveys the research objectives.

Weaknesses:

(1) Figure 2 displays representative FRAP images demonstrating fluorescence recovery within seconds. To gain a more comprehensive understanding of how recovery after photobleaching varies under different conditions, it is recommended to supplement these images with corresponding quantitative fluorescence recovery curves for analysis.

(2) Ostwald ripening typically leads to the shrinkage or even disappearance of smaller droplets, accompanied by the further growth of large droplets. However, the droplet size in Figure 2D decreases significantly after 2 h of incubation. This observation prompts the question, what is the driving force underlying RNA-regulated phase separation and phase transition?

(3) The manuscript aims to study the role of RNA in modulating PSMα3 aggregation by using solution-state NMR to obtain residue-specific structural information. The current NMR data, as described in the method and figure captions, were recorded in the absence of RNA. Whether RNA binding induces conformational changes of PSMα3, and how these changes alter the NMR spectra? Also, the sequential NOE walk between neighboring residues can be annotated on the spectrum for clarity.

(4) The authors claim that LL-37 shares functional, sequence, and structural similarities with PSMα3. However, no droplet formation was observed of LL-37 in the presence of RNA only. The authors then applied thermal stress to induce phase separation of LL-37. What are the main factors contributing to the different phase behaviors exhibited by LL-37 and PSMα3? What are the differences in the conformation of amyloid aggregates and the kinetics of aggregation between the condensation-induced aggregation in the presence of RNA and the conventional nucleation-elongation process in the absence of RNA for these two proteins?

https://doi.org/10.7554/eLife.109290.1.sa1

## Author response:

We thank the reviewers for their thoughtful and constructive comments, which greatly helped us to clarify, quantify, and strengthen both our findings and interpretations. Below, we provide a point-by-point response to each comment and describe the corresponding changes made.

> ***Public Reviews:***
>
> ***Reviewer #1 (Public review):***
>
> *Summary:*

> *The manuscript by Rayan et al. aims to elucidate the role of RNA as a context-dependent modulator of liquid-liquid phase separation (LLPS), aggregation, and bioactivity of the amyloidogenic peptides PSMα3 and LL-37, motivated by their structural and functional similarities.*
>
> *Strengths:*
>
> *The authors combine extensive biophysical characterization with cell-based assays to investigate how RNA differentially regulates peptide aggregation states and associated cytotoxic and antimicrobial functions.*
>
> *Weaknesses:*
>
> *While the study addresses an interesting and timely question with potentially broad implications for host-pathogen interactions and amyloid biology, several aspects of the experimental design and data analysis require further clarification and strengthening.*
>
> *Major Comments:*
>
> *(1) In Figure 1A, the author showed "stronger binding affinity" based on shifts at lower peptide concentrations, but no quantitative binding parameters (e.g., apparent Kd, fraction bound, or densitometric analysis) are presented. This claim would be better supported by including: (i) A binding curve with quantification of free vs bound RNA band intensities ,(ii) Replicates and error estimates (mean {plus minus} SD).*

We thank the reviewer for this suggestion. To quantitatively support the binding differences observed in Figure 1A, we have now performed densitometric analysis of the EMSA data and included the results in Figure S1. The analysis showed that the Kd for PSMα3 binding to polyAU and polyA RNA is in the same order of magnitude but lower for the polyAU, indicating a stronger binding. A description was added to the results in lines 137-145 of the revised version.

> *(2) The authors report droplet formation at low RNA (50 ng/μL) but protein aggregation at high RNA (400 ng/μL) through fluorescence microscopy. However, no intermediate RNA concentrations (e.g., 100-300 ng/μL) are tested or discussed, leaving a critical gap in understanding the full phase diagram and transition mechanisms.*

Our initial choice of 50 ng/μL (low RNA) and 400 ng/μL (high RNA) was guided by a broader RNA titration performed by turbidity measurements across 0, 10, 20, 50, 100, 200, and 400 ng/μL (Figure S2 in the revised version). In this screen, turbidity increased up to 50 ng/μL and then decreased dose-dependently from 100–400 ng/μL. We interpret this non-monotonic behavior as consistent with a transition from a dropletrich regime (maximal light scattering at intermediate dense-phase volume) toward conditions where assemblies become larger and/or more compact and sediment out of the optical path. This is described in lines 158-161 of the revised version.

Of note, additional intermediate RNA conditions (100 and 200 ng/μL) are included in Figure S14 (of the revised version). While these experiments were performed under the heat-shock perturbation, they nevertheless support the central point that RNA tunes assembly state across intermediate concentrations rather than producing a binary low/high outcome.

Importantly, we agree with the reviewer that a full phase diagram would be the most rigorous way to define the transition mechanism. However, establishing csat and constructing a complete phase diagram would require systematic measurements of dilute-phase concentrations (e.g., centrifugation/quantification or fluorescence calibration), controlled ionic strength titrations, and time-resolved mapping, which is beyond the scope of the present study. We have therefore revised the text to avoid implying that we provide a

complete phase diagram. Instead, we frame our results as a qualitative with multi-assay characterization showing that RNA concentration drives a shift from liquid-like condensates (at low RNA) toward solid-like assemblies (at high RNA), with an intermediate regime suggested by the turbidity transition and supported by additional imaging under stress. Finally, to address the "critical gap" concern directly, we add a sentence (lines 239-241) stating that: "Future work will be required to quantitatively define the phase boundaries and delineate the dominant mechanisms, such as sedimentation, dissolution, or coarsening/aging, across intermediate RNA concentrations.

> *(3) Additionally, the behaviour of PSMα3 in the absence of RNA under LLPS conditions is not shown. Without protein-only data, it is difficult to assess if droplets are RNA-induced or if protein has a weak baseline LLPS that RNA tunes. The saturation concentration (csat) for PSMα3 phase separation, either in the absence or presence of RNA, should be reported.*

In response to the reviewer's request, we have added Figure 2F, which shows PSMα3 alone in the absence of RNA under the same conditions. PSMα3 does not form droplets in this condition, indicating that condensate formation is RNA-dependent in the tested conditions. This is referred to in the text in lines 190-193 of the revised version. Please see our response about determining the csat in the response to the previous comment.

> *(4) For a convincing LLPS claim, it is important to show: Quantitative FRAP curves (mobile fraction and half-time of recovery) rather than only microscopy images and qualitative statements.*

We have included quantitative FRAP analysis in Figure S4 of the revised version, showing normalized recovery curves along with extracted mobile fractions and half-times of recovery ($t_{1/2}$). These quantitative measurements support the dynamic nature of the PSMα3–RNA. This is referred to in the text in lines 179-184 of the revised version.

> *(5) The manuscript highly relies on fluorescence microscopy to show colocalization. However, the colocalization is presented in a qualitative manner only. The manuscript would benefit from the inclusion of quantitative metrics (e.g., Pearson's correlation coefficient, Manders' overlap coefficients, or intensity correlation analysis).*

In response, we have added quantitative colocalization analysis to the revised manuscript. Specifically, we now report Pearson's correlation coefficients and Manders' overlap coefficients for the dual-channel fluorescence microscopy datasets in Figure S5 of the revised version. These metrics provide an objective measure of codistribution and complement the qualitative imaging.

The analysis supports that at low RNA concentrations (droplet/condensate conditions), PSMα3 and RNA show strong colocalization, consistent with RNA being incorporated within, or closely associated with, the peptide-rich phase. In contrast, at high RNA concentrations, where the assemblies are more solid-like/amyloid-positive, the quantitative coefficients decrease, consistent with reduced overlap and an apparent spatial demixing in which RNA becomes partially excluded from the peptide-rich structures. This is referred to in the text in lines 194-203 of the revised version.

> *(6) In Figures 3 B and 3C, the contrast between "no AT630 at 30 min, strong at 2 h" (50 ng/μL) and "strong at 30 min" (400 ng/μL) is compelling, but a simple quantification (e.g., mean fluorescence intensity per area) would greatly increase rigor.*

We have included quantitative analysis of AmyTracker630 fluorescence intensity in Figure S6 of the revised version, reporting the mean fluorescence intensity per area for the indicated conditions and time points. This quantification supports the qualitative differences observed

in Figures 3B and 3C. This is now referred to in the text in lines 233-236 of the revised version.

> *(7) In Figure S3 ssCD data, if possible, indicate whether the α-helical signal increases with RNA concentration or shows a non-linear dependence, which might link to the LLPS vs solid aggregate regimes.*

The ssCD spectra displayed in Figure S7 in the revised version (corresponding to Figure S3 in the original submission) show that the α-helical signature of PSMα3 is markedly enhanced in the presence of RNA compared to peptide alone, as evidenced by increased signal intensity, deeper minima, and more pronounced spectral features characteristic of α-helical structure. Importantly, this enhancement is more pronounced at 400 ng/μL Poly(AU) RNA than at 50 ng/μL, particularly after 2 hours of coincubation, indicating that RNA concentration influences the stabilization of α-helical assemblies. This is now more specifically detailed in the text in lines 258-263 of the revised version.

We note that solid-state CD does not allow direct quantitative deconvolution of secondary structure content (e.g., % helix) in the same manner as solution CD, due to sample anisotropy, scattering, and orientation effects inherent to dried or aggregated films. Consequently, our interpretation is qualitative rather than strictly quantitative. The ssCD data therefore suggest a non-linear dependence on RNA concentration, rather than a simple linear dose–response. This is also expected considering that phase transition, suggested by the other findings, is intrinsically non-linear.

> *(8) In Figure 5B, FRAP recovery in dying cells may reflect artifactual mobility rather than biological relevance. Additionally, the absence of quantification data limits interpretation; providing recovery curves would clarify relevance.*

We added quantitative FRAP analysis of the effect on PSMα3 within HeLa cells, shown in Figure S8 of the revised version. Compared to PSMα3 assemblies in vitro, nucleolar PSMα3 exhibits slower fluorescence recovery and a reduced mobile fraction. The nucleolus represents a highly crowded, RNA-rich cellular environment, which is expected to impose additional constraints on molecular mobility and likely contributes to the slower recovery kinetics observed in cells. This is now more specifically detailed in the text in lines 324-333 and discussed in lines 597-607 of the revised version.

> *(9) The narrative conflates cytotoxicity endpoints (membrane damage, PI staining, aggregates) with localization data (nucleolar foci), creating ambiguity about whether nucleolar targeting drives toxicity or is a consequence of cell death. Separating toxicity assessment from localization analysis, or clearly demonstrating that nucleolar accumulation precedes cytotoxicity, would resolve this ambiguity.*

We thank the reviewer for raising this important point. We agree that, in the current dataset, cytotoxicity readouts (membrane damage, PI staining, aggregate formation) and subcellular localization (nucleolar accumulation) are observed in close temporal proximity, which limits our ability to unambiguously assign causality. In the experiments presented here, PSMα3 was applied at concentrations known to induce rapid membrane disruption and cytotoxicity in HeLa cells. Under these conditions, PSMα3 accumulates on cellular membranes and penetrates into the cell and nucleus on very short timescales (seconds to minutes), likely preceding the temporal resolution accessible by standard live-cell fluorescence microscopy. As a result, nucleolar accumulation and cytotoxic endpoints are detected essentially concurrently, precluding a definitive determination of whether nucleolar association actively drives toxicity or occurs as a downstream consequence of membrane permeabilization and cell damage.

We therefore emphasize that, in this study, nucleolar localization is presented as a phenomenological observation consistent with RNA-rich compartment association, rather

than as a demonstrated causal mechanism of cytotoxicity. We have revised the Discussion (lines 597-607) to clarify this distinction and to avoid implying that nucleolar targeting is the primary driver of cell death.

We agree that resolving this ambiguity would require systematic time-resolved and concentration-dependent experiments, including analysis at sub-toxic PSMα3 concentrations below the membrane-disruptive threshold, combined with orthogonal imaging approaches. Such experiments are planned for future work but are beyond the scope of the present study.

> *(10) In Figure 8, to strengthen the LLPS assignment for LL-37, additional evidence, such as FRAP analysis or observation of droplet fusion events, would be valuable. This is particularly relevant given that the heat shock conditions (65 °C for 15 minutes) could potentially induce partial denaturation or nonspecific coacervation.*

In response to this comment, we have added FRAP analysis of LL-37 assemblies in the revised manuscript (Figure S12), including representative images and corresponding fluorescence recovery curves. The FRAP measurements show minimal fluorescence recovery over the acquisition window, indicating that the LL-37–RNA assemblies formed under these conditions are largely immobile and solid-like, rather than liquid-like droplets. This is now referred to in the text in lines 458-462 of the revised version.

> ***Reviewer #2 (Public review):***
>
> *In this paper, Rayan et al. report that RNA influences cytotoxic activity of the staphylococcal secreted peptide cytolysin PSMalpha3 versus human cells and E. coli by impacting its aggregation. The authors used sophisticated methods of structural analysis and described the associated liquid-liquid phase separation. They also compare the influence of RNA on the aggregation and activity of LL-37, which shows differences from that on PSMalpha3.*
>
> *Strengths:*
>
> *That RNA impacts PSM cytotoxicity when co-incubated in vitro becomes clear.*
>
> *Weaknesses:*
>
> *I have two major and fundamental problems with this study:*
>
> *(1) The premise, as stated in the introduction and elsewhere, that PSMalpha3 amyloids are biologically functional, is highly debatable and has never been conclusively substantiated. The property that matters most for the present study, cytotoxicity, is generally attributed to PSM monomers, not amyloids. The likely erroneous notion that PSM amyloids are the predominant cytotoxic form is derived from an earlier study by the authors that has described a specific amyloid structure of aggregated PSMalpha3. Other authors have later produced evidence that, quite unsurprisingly, indicated that aggregation into amyloids decreases, rather than increases, PSM cytotoxicity. Unfortunately, yet other groups have, in the meantime, published in-vitro studies on "functional amyloids" by PSMs without critically challenging the concept of PSM amyloid "functionality". Of note, the authors' own data in the present study, which show strongly decreased cytotoxicity of PSMalpha3 after prolonged incubation, are in agreement with monomer-associated cytotoxicity as they can be easily explained by the removal of biologically active monomers from the solution.*

We thank the reviewer for this important critique and agree that direct cytotoxicity is most plausibly mediated by soluble PSM species, while extensive fibrillation generally reduces toxicity by depleting these forms, a conclusion supported by our data and by other studies (e.g., Zheng et al 2018 and Yao et al 2019). We do not propose mature amyloid fibrils as the

primary toxic entities. Rather, we use the term functional amyloid in a regulatory sense, consistent with other biological amyloids whose fibrillar states modulate activity (e.g., hormone storage amyloids or RNA-binding proteins).

In line with emerging findings, we interpret PSMα3 toxicity as arising from a dynamic assembly process rather than from a single static molecular species. We previously showed that PSMα3 forms cross-α fibrils that are thermodynamically and mechanically less stable than cross-β amyloids and readily disassemble upon heat stress, fully restoring cytotoxic activity (Rayan et al., 2023). This behavior contrasts with PSMα1, which forms highly stable cross-β fibrils that do not recover activity after heat shock, suggesting that the limited thermostability of PSMα3 is an evolved feature enabling reversible switching between inactive (stored) and active states.

Consistent with this view, both PSMα1 and PSMα3 are cytotoxic in their soluble states, yet mutants unable to fibrillate lose activity, indicating that fibrillation is required but not itself the toxic end state (Tayeb-Fligelman et al., 2017, 2020; Malishev et al., 2018). Our other studies further show that cytotoxicity toward human cells correlates with inherent or lipid-induced α-helical assemblies, rather than with inert β-sheet amyloids (RagonisBachar et al., 2022, 2026; Salinas 2020, Bücker 2022). Together, these findings support a model in which membrane-associated, dynamic α-helical assembly, which requires continuous exchange between soluble species and growing fibrils, drives membrane disruption, potentially through lipid recruitment or extraction, analogous to mechanisms proposed for human amyloids such as islet amyloid polypeptide (Sparr et al., 2004).

In the present study, we further show that RNA reshapes this dynamic landscape: while PSMα3 alone progressively loses activity upon incubation, co-incubation with RNA preserves cytotoxicity by stabilizing bioactive polymorphs and condensate-like states, whereas high RNA concentrations promote solid aggregation but nevertheless preserve activity. Thus, aggregation is neither inherently functional nor toxic, but context-dependent and environmentally regulated. Taken together, our data support a model in which PSMα3 amyloids act as a dynamic reservoir, enabling *S. aureus* to tune virulence by reversibly shifting between dormant and active states in response to environmental cues such as heat or RNA.

This is now discussed in lines 56-76 and 523-553 of the revised version.

> *(2) That RNA may interfere with PSM aggregation and influence activity is not very surprising, given that PSM attachment to nucleic acids - while not studied in as much detail as here - has been described. Importantly, it does not become clear whether this effect has biologically significant consequences beyond influencing, again not surprisingly, cytotoxicity in vitro. The authors do show in nice microscopic analyses that labeled PSMalpha3 attaches to nuclei when incubated with HeLa cells. However, given that the cells are killed rapidly by membrane perturbation by the applied PSM concentrations, it remains unclear and untested whether the attachment to nucleic acids in dying cells makes any contribution to PSM-induced cell death or has any other biological significance.*

We thank the reviewer for this important point and agree that PSM–nucleic acid interactions are not unexpected and that our data do not support a direct intracellular role for RNA binding in mediating cytotoxicity. Accordingly, we do not propose nucleolar or nuclear association of PSMα3 as a causal mechanism of cell death. At the concentrations used, PSMα3 induces rapid membrane disruption, and nucleic acid association is observed along with membrane attachment, precluding conclusions about intracellular function. This limitation is now explicitly clarified in the revised manuscript. The biological significance of our findings lies instead in extracellular and environmental contexts, where PSMα3 encounters abundant nucleic acids, such as RNA or DNA released from damaged host cells or present in biofilms as

now addressed in lines 622631. Our data show that RNA modulates PSMα3 aggregation trajectories, shifting the balance between liquid-like condensates and solid aggregates, and thereby regulates the persistence and timing of cytotoxic activity. In this framework, RNA acts as a context-dependent regulator of virulence, rather than as an intracellular cytotoxic cofactor, an aspect which would be studied in depth in future work. This is now addressed in the text in lines 597-607 of the revised version.

> ***Reviewer #3 (Public review):***
>
> *Summary:*
>
> *The manuscript by Rayan et al. aims to investigate the role of RNA in modulating both virulent amyloid and host-defense peptides, with the objective of understanding their self-assembly mechanisms, morphological features, and aggregation pathways.*
>
> *Strengths:*
>
> *The overall content is well-structured with a logical flow of ideas that effectively conveys the research objectives.*
>
> *Weaknesses:*
>
> *(1) Figure 2 displays representative FRAP images demonstrating fluorescence recovery within seconds. To gain a more comprehensive understanding of how recovery after photobleaching varies under different conditions, it is recommended to supplement these images with corresponding quantitative fluorescence recovery curves for analysis.*

In response to this comment, we have supplemented the representative FRAP images with quantitative fluorescence recovery curves, reporting normalized recovery kinetics for the indicated conditions. These data are now provided in Figure S4 of the revised manuscript, allowing direct comparison of recovery behavior across conditions (shown by microscopy in Figure 2). In addition, we have included quantitative FRAP analyses for the cellular imaging shown in Figure 5 (presented in Figure S8) and for LL-37 assemblies formed under heat-shock conditions (Figure S12). Together, these additions provide a quantitative framework for interpreting the FRAP results and strengthen the distinction between liquid-like and solid-like assembly states.

> *(2) Ostwald ripening typically leads to the shrinkage or even disappearance of smaller droplets, accompanied by the further growth of large droplets. However, the droplet size in Figure 2D decreases significantly after 2 h of incubation. This observation prompts the question, what is the driving force underlying RNA-regulated phase separation and phase transition?*

We thank the reviewer for this observation. Across multiple samples, we consistently observe a coexistence of small droplets and larger aggregates, rather than systematic growth of larger droplets at the expense of smaller ones or a uniform decrease in droplet size. In addition, the timescales examined do not allow us to reliably assess whether diffusion-driven droplet coalescence is fast enough to draw firm conclusions about droplet size evolution. This is now addressed in the text in lines 181-184 of the revised version.

A decrease in droplet size over time is nevertheless observed in some instances and is more consistent with a time-dependent conversion of initially liquid-like condensates into more solid-like assemblies, which would reduce molecular mobility and suppress droplet coalescence. In parallel, progressive fibril formation may act as a sink for soluble peptide, leading to partial dissolution or shrinkage of less mature condensates. Together, these observations are consistent with a non-equilibrium aging process, in which RNAregulated

assemblies evolve from dynamic condensates toward more solid structures rather than following equilibrium Ostwald ripening.

> *(3) The manuscript aims to study the role of RNA in modulating PSMα3 aggregation by using solution-state NMR to obtain residue-specific structural information. The current NMR data, as described in the method and figure captions, were recorded in the absence of RNA. Whether RNA binding induces conformational changes of PSMα3, and how these changes alter the NMR spectra? Also, the sequential NOE walk between neighboring residues can be annotated on the spectrum for clarity.*

The solution-state NMR experiments were performed specifically to characterize the potential binding of EGCG to PSMα3. Due to the strong tendency of PSMα3 to undergo rapid aggregation and line broadening upon RNA addition, solutionstate NMR spectra in the presence of RNA could not be obtained at sufficient quality for residue-specific analysis. As suggested, we have updated and annotated the sequential NOE walk between neighboring residues on the relevant NOESY spectra to improve clarity.

> *(4) The authors claim that LL-37 shares functional, sequence, and structural similarities with PSMα3. However, no droplet formation was observed of LL-37 in the presence of RNA only. The authors then applied thermal stress to induce phase separation of LL-37. What are the main factors contributing to the different phase behaviors exhibited by LL37 and PSMα3? What are the differences in the conformation of amyloid aggregates and the kinetics of aggregation between the condensation-induced aggregation in the presence of RNA and the conventional nucleation-elongation process in the absence of RNA for these two proteins?"*

We appreciate this important question and have clarified both the basis of the comparison and the origin of the divergent phase behaviors of LL-37 and PSMα3. While PSMα3 and LL-37 share key properties as short, cationic, amphipathic α-helical peptides that self-assemble and interact with nucleic acids, they differ fundamentally in their assembly architectures. PSMα3 is an amyloidogenic peptide that forms cross-α amyloid fibrils, in which α-helices stack perpendicular to the fibril axis. In contrast, LL-37 can form fibrillar or sheet-like assemblies (observed in cryo grids), but these lack canonical amyloid features without clear cross-α or cross-β amyloid order, as so far observed by crystal structures. This is now clarified in different parts of the text of the revised version. Thus, the comparison between the two peptides is functional and physicochemical rather than implying identical amyloid mechanisms. These structural differences likely underlie their distinct phase behaviors.

Because LL-37 does not follow a classical amyloid nucleation–elongation pathway, and high-resolution structural information (e.g., cryo-EM) is currently lacking, partly due to its sheet-like, non-twisted morphology (unpublished results), it is not possible to directly compare aggregation kinetics or nucleation mechanisms between LL-37 and PSMα3. It is possible that amyloidogenic systems such as PSMα3 exhibit greater flexibility in prefibrillar and fibrillar polymorphism, enabling RNA-regulated phase behavior, whereas nonamyloid assemblies such as LL-37 are more prone to stress-induced solid aggregation. We note that this interpretation is necessarily tentative and does not imply a general rule, but rather reflects differences evident in the present system.

https://doi.org/10.7554/eLife.109290.1.sa0